Journal Pre-proof

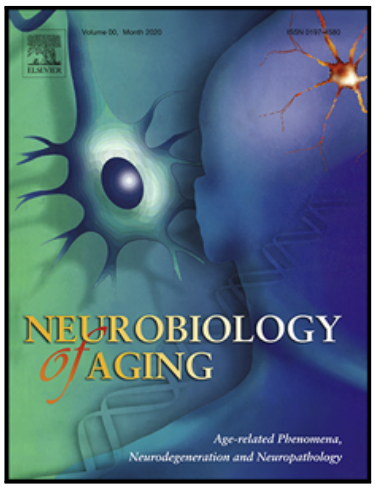

Evaluation of Early Microstructural Changes in the R6/1 Mouse Model of Huntington's Disease by Ultra-High Field Diffusion MR Imaging

Rodolfo G. Gatto , Carina Weissmann , Manish Amin , Quetzalli D. Angeles-López , Lucia García-Lara , Libia C. Salinas Castellanos , Daniel Deyoung , Jose Segovia , Thomas H. Mareci , Osvaldo D. Uchitel , Richard L. Magin

PII: S0197-4580(21)00056-7
DOI: https://doi.org/10.1016/j.neurobiolaging.2021.02.006
Reference: NBA 11077

To appear in: *Neurobiology of Aging*

Received date: 19 October 2020
Revised date: 4 February 2021
Accepted date: 7 February 2021

Please cite this article as: Rodolfo G. Gatto , Carina Weissmann , Manish Amin , Quetzalli D. Angeles-López , Lucia García-Lara , Libia C. Salinas Castellanos , Daniel Deyoung , Jose Segovia , Thomas H. Mareci , Osvaldo D. Uchitel , Richard L. Magin , Evaluation of Early Microstructural Changes in the R6/1 Mouse Model of Huntington's Disease by Ultra-High Field Diffusion MR Imaging, *Neurobiology of Aging* (2021), doi: https://doi.org/10.1016/j.neurobiolaging.2021.02.006

Highlights

- Ultra-high field diffusion MRI can detect brain changes in the R6/1 mouse model.
- DTI captures early microstructural changes across different brain structures.
- NODDI provides parameters linked to early neuroinflammatory markers.

Evaluation of Early Microstructural Changes in the R6/1 Mouse Model of Huntington's Disease by Ultra-High Field Diffusion MR Imaging

*Rodolfo G. Gatto[1]†, Carina Weissmann[2]†, Manish Amin[3]†, Quetzalli, D. Angeles-López[4], Lucia García-Lara[4], Libia C. Salinas Castellanos[4], Daniel Deyoung[3], Jose Segovia[4], Thomas H. Mareci[3], Osvaldo D. Uchitel[2], and Richard L. Magin[1]

[1] *Department of Bioengineering, the University of Illinois at Chicago, Chicago, IL USA.*

[2]*Insituto de Fisiología Biología Molecular y Neurociencias-IFIBYNE-CONICET, Universidad de Buenos Aires, Argentina.*

[3]*Department of Biochemistry, National High Magnetic Field Laboratory, Gainesville, Florida, US.*

[4]*Departamento de Fisiología, Biofísica y Neurociencias, Centro de Investigación y de Estudios Avanzados del IPN, México City, México.*

† Authors contributed equally to this work.

ABSTRACT

Diffusion MRI (dMRI) has been able to detect early structural changes related to neurological symptoms present in Huntington's disease (HD). However, there is still a knowledge gap to interpret the biological significance at early neuropathological stages. The purpose of this study is two-fold: (i) establish if the combination of Ultra-High Field Diffusion MRI (UHFD-MRI) techniques can add a more comprehensive analysis of the early microstructural changes observed in HD, and (ii) evaluate if early changes in dMRI microstructural parameters can be linked to cellular biomarkers of neuroinflammation. Using an ultra-high field magnet (16.7T), diffusion tensor imaging (DTI), and neurite orientation dispersion and density imaging (NODDI) techniques were applied to fixed *ex-vivo* brains of a preclinical model of HD (R6/1 mice). Fractional anisotropy (FA) was decreased in deep and superficial grey matter (GM) as well as white matter (WM) brain regions with well-known early HD microstructure and connectivity pathology. NODDI parameters associated with the intracellular and extracellular compartment, such as intracellular ventricular fraction (ICVF), orientation dispersion index (ODI), and isotropic volume fractions (IsoVF) were altered in R6/1 mice GM. Further, histological studies in these areas showed that glia cell markers associated with neuroinflammation (GFAP & Iba1) were consistent with the dMRI findings. dMRI can be used to extract non-invasive information of neuropathological events present in the early stages of HD. The combination of multiple

imaging techniques represents a better approach to understand the neuropathological process allowing the early diagnosis and neuromonitoring of patients affected by HD.

Keywords

Huntington's disease; Ultra-high Field Diffusion MRI; R6/1 Mice; Diffusion Tensor Imaging; Neurite Orientation Dispersion and Density Imaging; Neuroinflammation.

1. INTRODUCTION

Huntington's disease (HD) is a hereditary neurodegenerative disease most recognized by slow and progressive abnormal movements that were noted in the 19th century and described in detail by George Huntington (Walker, 2007). As such, HD is associated with a distinct phenotype, including chorea and dystonia, incoordination, cognitive decline, and behavioral difficulties. The genetic mutation of the huntingtin (*HTT*) gene is responsible for an atypically long polyglutamine (poly Q) expansion in the huntingtin (HTT) protein (Finkbeiner, 2011). Such polyQ expansion (more than 35 CAG repeats) makes HTT prone to misfolding, aggregating, and accumulate (Zheng and Diamond, 2012). Eventually, this leads to neurodegeneration, particularly in medium spiny neurons (MSNs) of the grey matter (GM) nuclei of the striatum (STR) which has been well described (Vonsattel et al., 1985). HD is particularly devastating due to its multiple cognitive features, which have a relentless course of over 10–20 years. Such early HD symptoms have been attributed to an impairment in the frontal cerebral cortex (particularly layers III, V, and VI) (Zheng and Diamond, 2012). However, new evidence suggests that other brain areas might be involved, particularly the hippocampus, which has been under analysis in different mouse models and HD patients (Begeti et al., 2016; Harris et al., 2019; Quirion and Parsons, 2019). Unfortunately, there are no current therapeutic strategies to stop or slow down the disease progression, and fatality frequently occurs about 20 years after diagnosis (Roze et al., 2010).

Advancements in MRI techniques have opened a new window of preclinical microstructural exploration in neuroanatomical regions particularly susceptible to HD (Shim et al., 2019). Current improvements in gradient fields and imaging resolution have been able to non-invasively capture features, with improved accuracy *in vivo* and *ex vivo* at the early stages of neurodegenerative diseases (Gatto et al., 2018a; Gatto et al., 2018b; Muller et al., 2020). The development of new diffusion MRI techniques has opened a new realm with a great number of parameters associated with microstructural anomalies in HD (Rosas et al., 2006). Diffusion tensor imaging (DTI), a mono-exponential Gaussian imaging technique, has been applied to obtain parameters mostly related to WM changes during the disease in mouse models (Douaud et al., 2009; Gatto, Rodolfo G. et al., 2020; Magnotta et al., 2009), whereas other more complex models like neurite orientation dispersion and density imaging (NODDI) are contributing with additional information in different diseases at the clinical level (Kamiya et al., 2020), with few but growing number of examples in the context of HD of preclinical models. Thus, a more comprehensive approach combining the different diffusion MRI techniques could be applied to increase our understanding of the intricate cellular changes in the early stages of HD.

Murine models are the most widely used to study HD, based on their availability and practical use (Figiel et al., 2012; Switonski et al., 2012). Initial manipulation of the transgenic founder line (R/6 mouse) led to the R6/1 mice that express exon 1 of the human gene (*HTT*) carrying a 115 CAG repeat, which has been previously characterized and widely used to test therapeutic compounds (Naver et al., 2003). Aggregates/inclusions have been detected in the striatum around 8 weeks of age (Li et al., 2005). Additionally, no qualitative evidence of massive cell death in the R6/1 mice was found in the model (Naver et al., 2003). Also, a longitudinal study showed that overall, striatal, cortical, and hippocampal volumes were different between WT and R6/1 mice as well as age-related deficits in both motor and cognitive behaviors detectable by 11 weeks of age. However, no detectable associations between mHTT load and MRI-based regional brain changes were identified (Rattray et al., 2013). The slower progression of the disease in the R6/1 mouse makes it more suitable for investigating the long-term effects of treatments, as well as for

analyzing changes in both, the presymptomatic as well as in the symptomatic state (Gatto and Weissmann, 2019). Thus, the evaluation of these models using different imaging techniques in the field of HD could help interpret MRI findings and early neuropathological mechanisms.

One of the central mechanisms involved in HD neuronal death is neuroinflammation; reactive inflammatory processes are one of the most studied at the early stages of HD (Politis et al., 2015). The activation of the components of the glia, particularly astrocytes with HTT inclusions have been detected and related to alterations in HD (Cisbani and Cicchetti, 2012). Thus, the evaluation of early associated neuroinflammatory biomarkers in physiological intact organisms is paramount to move research in this field forward. Overall, the purpose of this study is two-fold: (i) combine different diffusion techniques and add a more comprehensive insight into the early microstructural changes observed in HD; (ii) evaluate if early microstructural changes are linked to cellular markers of neuroinflammation. To the best of our knowledge, this is the first study using microstructural multi-modality imaging methods in the R6/1 transgenic animal model of HD.

2. MATERIAL AND METHODS

2.1. Animals

All animal procedures were performed according to the Guide for the Care and Use of Laboratory Animals, as adopted by the US National Institutes of Health, the Mexican Regulation of Animal Care and Maintenance (NOM-062-ZOO-1999, 2001), and in agreement with internal Cinvestav regulations. Mice had easy access to food and water and were checked daily to assess their level of well-being and health. Mice had *ad libitum* access to food and water in aseptic conditions with climate and light-controlled system and were checked daily to assess their level of well-being and health. R6/1 mice were obtained from Jackson Laboratories (stock #002809) with a C57BJ6 background, overexpressing 115 ± 6 CAG repeats. Mice were genotyped by end-point PCR based on previous protocols (Segovia, 2002). To amplify the mutant fragment of the human huntingtin gene we used the following

primers: forward 5´ GCA GCA GCA GCA GCA ACA GCC GCC ACC GCC, and reverse 5´ CGG CTG AGG CAG CAG CGG CTGT. To reproduce our results with more biological accuracy (as well as for future translational and reproducibility purposes), a mixed pool of male and female mice was used in this study, as has been previously done (Beery, 2018; Xiang et al., 2011). The R6/1 mice have been previously characterized and they develop motor symptoms between 14 to 20 weeks of age and die around 48 weeks (Ferrante, 2009). After a proper review of the literature, among the two-common method of sample size calculation in animal studies (Charan J et al 2013), A power analysis approach was used to calculate the sample size for a significance level (type 1 error) fixed at the level of 5%(p=0.05) and a power (β) <0.80 (Charan and Kantharia, 2013; Dattalo, 2018).

To disentangle alterations due to HD progression from normal aging, we initially considered two control groups of C57/BJ6 mice to match the experimental groups at the early presymptomatic stage of 11 weeks (P77), and a late R6/1 symptomatic group at postnatal week 30 (P320) with a total of 16 animals used: wild type (WT) controls and R6/1 mice (n=4 per group). No significant differences were detected between both control groups.

2.1. Animal preparation for MRI imaging

Animals were deeply anesthetized with an overdose of pentobarbital sodium, then transcardially perfused with PBS and 4% paraformaldehyde (PFA) solution. After the skull was opened, mouse brains were extracted intact and immersed in PFA (> 48 hours). Before scanning, brains were soaked overnight in PBS to remove free fixative. Brain stacks (3) were placed in 10 mm diameter NMR tubes (New Era #NEML10-7, 300-400 MHz) and the tubes were filled with fluorocarbon oil (Fluorinert®, 3M, Maplewood, MN) and gently stabilized using coronoid tips. Three (3) 10mm tubes were gently placed in a 25mm coil. Images from all brains were acquired with a 17.6 T vertical-bore Avance II scanner using a 25-mm RF coil, Micro-2.5 gradients, and Paravision 6.0 software (Bruker, Karlsruhe, Germany). The brain settings allowed the placement of a stack of 3 brains per 10mm MRI compatible tubes.

2.3. MR image acquisition and processing

Two (2) MRI scans sessions (involving 6 mice brains each) were performed (total mouse brains N=12). Three (3) experimental groups (WT pre and symptomatic control, R6/1(11weeks presymptomatic), and R6/1 symptomatic (30 weeks), coronally centered and oriented along the rostral-caudal axis of each brain (n=4 per animal group). A total of 170 MRI slices were acquired using a spin-echo sequence with TR= 10000 ms and TE =20 ms, interleaved 0.2 mm thick slices, with a field of view = 25 x25 x 34 mm^3 in each block of slices, in-plane acquisition matrix = 125x125x170, for an isotropic image resolution of 200 microns, b = 0 s/mm^2 for each shell: b = 1000 s/mm^2 in 20 directions, and b = 2500 s/mm^2 in 64 directions, with 3.5 ms duration (δ) and 11 ms of separation (Δ) of the gradient pulses. This acquisition was averaged twice for a total time of approximately 19 hrs. per set in the cool bore (20 degrees Celsius) of the 17.6 T magnet (750 MHz/89 mm Bruker Avance III HD). Due to the potential hardware vibrations, and field inhomogeneity, susceptibility corrections were performed. All the DWIs to the baseline image (b0), correction of the eddy currents, as well as motion and artifacts corrections were accounted for using standard preprocessing procedures (Andersson et al., 2003; Andersson and Sotiropoulos, 2016). DTI parameters data processing was performed using FSL (Jenkinson et al., 2012) to calculate fractional anisotropy (FA).

For NODDI calculations, we followed the MATLAB scripts provided in (Zhang et al., 2012). For NODDI fitting, the initial condition for the intrinsic diffusivity (D_{in}) of the neural tissue was set to 0.6 x 10^{-3} mm^2/s, particularly optimized for an overall murine brain tissue as described in earlier work (Wang et al., 2019). A default value of isotropic diffusivity (2.0 × 10−3 mm2/s) was used for D_{iso} value as indicated in previous studies (Holz et al., 2000). Applying equations already implemented in the original MATLAB algorithms in ex vivo fixed tissue, an additional dot-compartment (diffusion is restricted in all directions) was included for the fitting. (Dhital et al., 2018). Manual segmentation, volumetric calculations, and diffusivity parameters were acquired for three different brain structures: a) Superficial GM cortical areas (superficial GM), b) subcortical areas (deep GM); and c) WM tracts, using ITK-SNAP (www.itksnap.org) (Yushkevich et al., 2006; Yushkevich et al., 2016). Regions of interest (ROIs) were manually defined following stereotaxic coordinates and landmarks presented by the Paxinos mouse brain atlas

(Paxinos and Franklin, 2004). Four (4) superficial GM ROIs areas were selected; frontal accessory cortical area (FrAc), the Cingular cortex (Cing), the primary motor cortex (M1), and the supplementary motor cortex (M2). Two (2) deep GM areas were selected; the striatum (STR) and the hippocampus (HC). Additionally, we analyzed the corpus callosum (CC), a WM area generally affected by HD disease (Gatto and Weissmann, 2019; Phillips et al., 2013; Phillips et al., 2014).

For tractography reconstructions and exploration purposes, a multi-shell diffusion scheme was used, with the b-values of 1000 and 2500 s/mm^2 and sampling directions used were 20, and 20, respectively. The in-plane resolution was 0.15 mm. The slice thickness was 0.15 mm. The b-table was checked by an automatic quality control routine to ensure its accuracy (Schilling et al., 2019). The diffusion tensor was calculated. A deterministic fiber tracking algorithm (Yeh et al., 2013) was used. A seeding region was placed at the whole brain with a volume size of 4.2e+02 mm$^{3.}$ The ROI was placed in the striatum region with a volume size of 5 mm^3. The anisotropy threshold was 0.0960938. The angular threshold was 90 degrees. The step size was randomly selected from 0.5 to 1.5 voxels. The fiber trajectories were smoothed by averaging the propagation direction with a percentage of the previous direction. The percentage was randomly selected from 0% to 95%. Tracks with a length shorter than 0 or longer than 20 mm were discarded. A total of 50000 seeds were placed. ROIs were used for brain parcellation, and the connectivity matrix was calculated by using the count of the connecting tracks. The connectivity matrix and graph theoretical analysis was conducted using DSI Studio (http://dsi-studio.labsolver.org).

2.4. Immunohistochemistry

After MRI scanning, oil media was removed, and brains were placed in increasing concentration of sucrose solutions [5-30 %] for an additional 24 hrs for cryo-protection. After embedding in optical cutting temperature (OCT) polymer compound (Tissue Tek, Sakura, Finetek, cat #4583), 50 µm thick brain sections were obtained using a microtome (Leica cryostat CM 1850 Cryostat, Buffalo Grove, IL). Brain sections were mounted on slides (Fisher-brand Superfrost, cat# 12-550-15) and dried for 15 minutes. Then, the OCT was removed by washing three times with Tris base buffer (TBS) and permeabilized with 0.25% Triton x-100 (20 min) and treated with blocking solution (1% BSA, 0.01% Triton x-100 in TBS) for an hour at room temperature (RT). Slides were incubated then

with the primary antibody overnight in blocking solution, washed in TBS, and incubated with the secondary antibody for 60 min in blocking buffer. After washing, slides were incubated in propidium iodide (PI) for 15 min to detect nuclei. After a final wash in TBS, slides were dried and mounted in Vecta-Shield mounting media (Vector Laboratories, Burlingame, CA). The antibodies used were rabbit polyclonal antibody against glial fibrillary acid proteins (GFAP) (DAKO, Glostrup, Denmark; 1:700), mouse monoclonal against (Ionized calcium-binding adaptor molecule 1 (anti-Iba1) (Wako, 019-19741, 1:200). PI (Molecular Probes) 20 mM was used in a solution 10 uM in TBS containing Tx-100 (0.01%) and RNAse.

Cortical and hippocampal images in mice were acquired with an Olympus FV300/BX61 microscope. Alexa-647 and Alexa-488-conjugated secondary antibodies, and PI were excited using Argon (lambda: 488 nm), Helium-Neon (lambda: 543 nm), Helium-Neon (lambda: 633 nm) lasers, and a transmission light detector as previously described (Castellanos et al., 2020). For quantitative experiments, identical laser power and acquisition settings were used. Representative histological sections were selected matching stereotaxic coordinates using MRI brain imaging (The Mouse Brain: 1st Ed, Watson & Paxinos, 2008). Measurements were done using open-source ImageJ software (Collins, 2007; Schneider et al., 2012). Mean intensity values were used for quantitative purposes. Four representatives (4) ROIs from four (4) consecutive immunohistochemistry (IHC) slides (n=16 ROIs) were selected for analysis (Gatto, R. G. et al., 2020). In the case of CA1, CA3, and DG areas, ROIs were selected from the PI channel to determine the different layers (pyramidalis, radiata) and mean grey values obtained (background corrected) from the antibody channel (n=15-20 ROIs) in an analysis similar to that performed by Ugolino et al. (Ugolini et al., 2018). For fractal and branch analysis, we used the plugin FracLac and Skeleton respectively in ImageJ. The analysis performed was similar to that described by Young et al (Young and Morrison, 2018). Representative fluorescent micrographs were increased in brightness and contrast equally for all conditions (WT, presymptomatic, and symptomatic) to visually show the differences mentioned in the legends.

2.5. Statistical analysis

Quantitative data were tabulated and analyzed using GraphPad Prism version 6 software (La Jolla, CA). According to animal protocols, a minimum group size of animals was established using power analysis and sample size calculations based on the results from previous pilot work (Gatto et al., 2015). Multiple comparison corrections using the false discovery rate (FDR) method were performed (Benjamini, 2010; Benjamini and Hochberg, 1995). For quantitative analysis, one-way ANOVA and Tukey's post-hoc tests were used to determine statistical differences among different experimental animal groups. A value of $p < 0.05$ was used to demonstrate statistical significance. Additionally, non-parametric statistical tools (Mann–Whitney test) were used. Error bars in all tables represent the standard error of the mean (s.e.m.). In the graphs, data are visualized as box plots representing the median value and whiskers representing the upper (25%) and lower (75%) quartile.

RESULTS

3.1. UHFD-MRI can capture volumetric changes in GM cortical areas of the R6/1 mice.

Presymptomatic (11 weeks) and symptomatic (30 weeks) R6/1 and control animal brains were scanned to analyze the different regions shown in **Fig. 1**. As illustrated in **Fig. 2**, volumetric changes were captured in different segmented areas. Whole-brain volumes were significantly reduced in symptomatic R6/1 compared to WT controls (WT-11wks) = 422.8 ± 17.2 mm^3 vs R6/1 (30wks) = 366.8 ± 7.27 mm^3, $p<0.02$) (13.3 % decrease), but not in the presymptomatic mice group (R6/1 (11wks) = 380.3 ± 5.26 mm^3, $p<0.05$) (9.9 % decrease). In specific WM regions, like the corpus callosum (CC), a significant reduction was attained only in the R6/1 symptomatic group (WT-11wks = 13.7 ± 0.5 mm^3 vs R6/1 (30wks) = 11.1 ± 0.4 mm^3, $p<0.02$) (18.97 % decrease). In deep GM regions, like the striatum (STR) and hippocampus (HC), only significant changes were seen in the symptomatic stages (STR, WT-11wks = 33.7 ± 2.62 mm^3 vs. R6/1 (30wks) = 24.9 ± 2.4 mm^3, $p<0.04$), (HC, WT-11wks) = 22.0 ± 0.3 mm^3 vs. R6/1 (30wks) = 18.3 ± 1.3 mm^3, $p<0.03$) with a decrease of 26.1% and 16.8% respectively. Changes were also detected in M1 and M2 motor cortex areas at the symptomatic stage. In other areas of the cortex (CCX), such as the frontal accessory (FrAc) (WT-11wks = 13.9 ± 2.3 mm^3 vs R6/1 (11wks) = 7.35 ± 0.45 mm^3, $p<0.02$) (47.1% decrease), and cingulate cortex (Cing) (WT-11wks = 7.57 ± 0.52 mm^3 vs R6/1 (11wks) = 5.0 ± 0.57 mm^3, $p<0.01$) (33.97%

decrease), significant presymptomatic volumetric decreases were accounted for. Additional normalization of each brain structure by the total brain volume on each experimental group and effect size analysis (Daly and Cohen, 1987; Rosenthal and Rosnow, 1984) is shown in **Supplementary Table 1**. These results show that the R6/1 model depicts changes as already described in other HD mouse models and was further analyzed.

3.2. Enlargements of the R6/1 mice ventricular system can be detected by UHFD-MRI.

An increase in ventricular volumes was observed in the R6/1 mice compared to the WT control group **(Fig.3)**. These changes were substantially larger for the lateral (WT-11wks = 1.49 ± 0.07 mm^3, vs. R6/1 (11wks) = 1.62 ± 0.05 mm^3 vs. R6/1 (30wks) = 5.18 ± 0.28 mm^3) and third ventricular systems (WT-11wks = 2.23 ± 0.08 mm^3 vs. R6/1 (11wks) 2.33 ± 0.09 mm^3, vs. R6/1 (30wks) = 3.13 ± 0.13 mm^3) than in the fourth ventricle (WT-11wks = 1.09 ± 0.05 mm^3 vs. R6/1 (11wks) = 1.30 ± 0.11 mm^3 vs. R6/1 (30wks) = 1.45 ± 0.17 mm^3). However, statistical significance was only attained between control and R6/1 groups at later stages (lateral ventricle: WT-11wks vs. R6/1 (30wks), $p<0.0001$), (third ventricle; WT-11wks vs. R6/1 (30wks), $p<0.001$) and (fourth ventricle; WT-11wks vs. R6/1 (30wks), $p<0.01$). These findings agree with those described in other HD mouse models and thus moved us forward to detect additional changes via contributing MRI techniques.

3.3. DTI can detect early microstructural anomalies in the R6/1 mice.

In WM tracts particularly affected in the context of HD (like the CC). the averaged FA reached a significant reduction in presymptomatic animals (11 weeks), specifically in its anterior portion or genu **(Fig.4,5a)**. However, no other significant changes in FA were seen in the CC body or splenium regions. Analysis of the striatum showed a spread increase of FA across the entire region as the disease progressed towards the symptomatic stage **(Fig.4,5b)**. Moreover, the hippocampus showed an early initial localized FA decrease in the middle (numbered as "HC plane 2" in **Fig.1**) spreading to its entire region at the symptomatic stage **(Fig.4,5c)**. Cortical FrAc and Cing regions **(Fig.4,5d)**, presented a broader change between normal and disease groups at the very early presymptomatic period

fundamentally located to the more anterior portions of the brain. Cortical areas, as the M1 and M2, showed more modest and localized early reductions in FA as well. A more detailed account of DTI derivatives from the segmented ROIs, including axial (AD = λ_1), radial (RD = $\lambda_2 + \lambda_3$)/2, and mean diffusivity (MD = $\lambda_1 + \lambda_2 + \lambda_3$)/3) are described in **Table 1.** Analysis of brain diffusion tensor maps, as well as deterministic tractography reconstructions, have shown a significant and progressive loss in terms of axonal connectivity in the R6/1 mice groups, compared to the WT control **(Fig. 6,7)**.

3.4. Changes in brain tissue compartments can be detected by NODDI parameters.

Using NODDI as a multi-shell technique in our R6/1 mouse model, we were able to determine changes in intra-neurite, extra-neurite, and free water compartment (Zhang et al., 2012). In the genu portion of the CC, we observed a significant decrease in the intracellular volume fraction (ICVF) at the HD presymptomatic and symptomatic stages, as well as an increase in the orientation dispersion index (ODI), and the isotropic volume fraction (IsoVF) **(Fig. 8a)**. In cortical FrAc and Cing areas, a progressive increase in symptomatic values of IsoVF was detected, as well as in subcortical GM structures. However, in the HC, IsoVF changes were seen more prevalent in the presymptomatic than the symptomatic phase of the disease **(Fig. 8b)**. A complete recollection of the changes in NODDI parameters across each segmented ROI is shown in **Table 2**.

3.5. Early cellular neuroinflammatory structural biomarkers in the R6/1 mouse brain.

The presence of early glia anomalies in HD has been documented in previous work. In this preclinical model, we evaluated the presence of GFAP as a maker to track astrocytes. Our studies found increased levels of this protein as the disease progressed, in susceptible structures, such as the CCX, CC, and STR of the presymptomatic R6/1 mice compared to the WT control (**Fig. 9a, b, c)**. These results were larger in the middle HC region, particularly early stages **(Fig. 9d)**.

A more thorough examination of the different regions of the HCs is shown in **Fig. 10**. The HC was subdivided into different areas, and ROIs in each were established to determine the intensity of the GFAP signal, the number of astrocytes, and morphological alterations **(Fig. 10a, b, c)**. The plots show that the intensity of the GFAP signal was higher in all areas (CA1, CA3, and hilus) for the symptomatic animals. Interestingly, the CA3 area showed the highest GFAP signal for presymptomatic animals, similar to what was observed for FA values in HC middle portions **(Figs. 5 and 6**). We focused on the CA3 area for further analysis. A higher density of astrocytes was evidenced in the R6/1 presymptomatic mice compared to the WT control or symptomatic counterparts **(Fig. 10b, bottom)**. Additionally, we performed a structural analysis using skeletonizations and fractals to compare the cell morphologies (**Fig. 10c**, explained in materials and methods). The parameters obtained, the fractal dimension (FD) and lacunarity (L) offer a way of quantifying and comparing geometrical complexity (Di Leva, 2016) and have been used extensively in the field of neuroscience as well as many others (Kapitulnik and Deutscher, 1984). In general terms, a higher FD reflects a higher irregularity, while L complements the analysis yielding a measure of heterogeneity. The representative astrocyte images show a higher FD (fractal dimension) and L (lacunarity) in the R6/1 compared to WT-11wks mice evidencing a higher level of complexity, even at the presymptomatic stage.

The microglia (stained with Iba1) has been documented as playing a role at the later stages of HD (Palpagama et al., 2019). Results from our analysis confirmed this with a significant increase in the levels of the marker located in the medial areas of the HC at the presymptomatic stage of the R6/1 compared to the WT-11wks control mice **(Fig. 11)**.

4. DISCUSSION

This work has revealed early changes in dMRI microstructural parameters in the R6/1 HD mouse model and associated the findings with cellular biomarkers of neuroinflammation. At the macrostructural level, changes in volumes detected in this work **(Fig. 2)** are in line with those determined in HD patients, and documented in other HD mouse models, like the zQ175 (Heikkinen et al., 2012) and previous work in the R6/1 mice (Hansson et al.,

1999). Other HD mouse models show volumetric changes as well. In the case of the R6/2 model, changes were detected via MRI in symptomatic animals, CCX, STR, and HC, but not in presymptomatic animals (Cepeda-Prado et al., 2012). Volume loss was also detected in the HdH150Q mouse brain at pre-and post-symptomatic stages (Steventon et al., 2016). In this study, R6/1 mice mimic changes described in clinical HD, with a volume loss of about 23% in total cortical GM (Halliday et al., 2009), and highest in STR nuclei (Ruocco et al., 2006).

An increase in HD ventricular size is another main feature described in HD (Hobbs et al., 2010). Likewise, preclinical studies in rodent models of NDDs have shown that the detection of changes in ventricular size measured by UHF-MRI is feasible. In clinical longitudinal MRI studies, Hobbs et al. estimated that HD ventricular volumes (adjusted for normal aging, sex, and total intracranial volume) increased more than in control groups, only one year before the onset of motor deficits (Hobbs et al., 2010). This short window of presymptomatic detection agrees with our findings **(Fig.3),** where no significant changes in the R6/1 mouse were seen at an earlier stage of the disease. This finding confirms the fact that ventricular size is not a reliable bioimaging marker to predict HD at earlier stages.

At the microstructural level, (among the effects associated with the presence of mutant HTT), the loss of axonal connectivity (AC) is one of the earliest and main pathological events described in HD (Cowan and Raymond, 2006; Sieradzan and Mann, 2001). This AC loss can be visualized further with the use of MRI techniques in preclinical models, like the R6/1 mice **(Table 3)**. dMRI has shown that DTI can evaluate brain injury and reveal changes in brain microstructure (Gupta et al., 2008; Gupta et al., 2010; Gupta et al., 2012). FA values reported in this work **(Fig. 5, 6)** agree with the literature: as the progression of the disease relates to structure disorganization, we found lower FA values in WM and superficial GM structures - as well as opposite increased FA values in deep GM nuclei (STR). The unexpected increase of FA in the striatum might reflect a coherent breakdown of different grey and white matter constituents (e.g., microstructure simplification, cytoskeleton degeneration, myelin breakdown, loss of

cortical axons (Fazio et al., 2018). Also, as Douaud et al suggested, an atypical increase of FA could be the result of the selective loss of some of the subcortical connections targeted by the degenerative process–i.e., mainly the striatopallidal projections at an early stage of the disease that may turn the striatum into a seemingly more organized structure (Douaud et al., 2009) and reviewed before (Gatto and Weissmann, 2019). This reinforces the validity of the R6/1 as a model to further evaluate changes in HD. Moreover, specific delineation of anterior to posterior regions, within the structures of interest detected the longitudinal progression of the disease. Such changes in neuronal connectivity can be reflected in WM orientations, probably related to a balance of several factors such as neurodegeneration and microstructure reorganization, as well as neuroplastic events (Gatto, 2020b). This is also detected in this study by the significant changes in DTI parameters (FA) and changes in the histological compartments determined by NODDI (ICVF and particularly ODI). This new information can improve our understanding of the topographic evolution of the disease and network alterations at the different stages **(Fig.7)**, as described in other preclinical models of HD (Chang et al., 2018).

Anomalies described by DTI can be connected to AC changes **(Table 1)**. However, the study of neuroinflammation requires a dual intra and extracellular analysis. In the NODDI model, ODI parameters (and by extension ICVF and IsoVF scalars) have been directly related to the loss of connectivity and neuroinflammation phenomena. As an example, Yi et al. showed that the increased presence of microglia in the extra-neurite space contributed to alterations in water diffusivity, particularly detected in ODI values (Yi et al., 2019). An extra-neuronal compartment upsurge (based on an increase in ODI values) in the context of microglia infiltration, would be somehow difficult to explain. In this work, NODDI results not only reproduced the compartmental redistribution measured by ICVF and ODI in other NDDs (Gatto et al., 2018c) **(Table 2)**. The alteration of other parameters associated with an increase of free water in the interstitial space (IsoVF) could more accurately represent the increase in interstitial water associated with inflammatory processes. This has been described in other neurodegenerative diseases (Gatto et al., 2018c) and depicted in **(Fig.8b**).

Our work detected a marked change in the diffusion change in the middle portion of the HC at a presymptomatic stage. The same area showed changes as detected in our histological studies using neuroinflammatory markers and centered in the HC middle portion, particularly in the CA3 region (**see Fig. 9**). Glial (and diffusion) changes in HC could relate to cognitive alterations documented in clinical and rodent models, showing an increase of GFAP levels in CA1, CA3, and DG regions (Bondan et al., 2019). Additionally, studies have shown that structures such as the HC is particularly sensitive to the harmful effects of neuroinflammatory mechanisms in synaptic plasticity (Mancini et al., 2017). Detailed histological analysis in HC showed changes in astrocyte morphology, a common pathological feature preceding structural deficit that may drive disease progression. Astrocytes undergo a series of morphological and functional changes (overall described as astrogliosis) mainly characterized by swelling of the cell body, presence of larger and thicker processes, as well as increasing GFAP-expression (Pirici et al., 2009). Also, this cell type expresses AQP-4 channels and thus their role in water uptake as has been described for other NDDs (Gatto et al., 2018a). Specifically, in HD, astrocytes show inclusions of mutant HTT (mHTT) proteins that have been related to alterations of its components (Cisbani and Cicchetti, 2012; Shin et al., 2005). This alone was shown to trigger HD pathology in mice that overexpress mHTT exclusively in astrocytes (Bradford et al., 2010).

In our MRI experiments, isoVF showed alterations in HC middle portions at the early stages; interestingly, histology showed that GFAP increased levels were also prominent particularly in CA3 areas of the HC together with an increase in astrocyte complexity. Likewise, differences in GFAP levels in different areas of HC were also described for Alzheimer's disease (AD) transgenic mice compared to the WT counterpart (Ugolini et al., 2018), and a change in astrocytic morphology was reported also in some brain structures of the R6/2 mice (Vorisek et al., 2017). In previous work, astrocytes have been analyzed via the fractal dimension (FD) in different preclinical (Reichenbach et al., 1992), and clinical studies (Pirici et al., 2009). In our studies, we found that different conditions (control, presymptomatic and symptomatic mice) bore differences in astrocytic morphological patterns **(Fig.10)**.

PFA fixation has an impact on diffusion parameters. As an example, clinical studies have shown that formalin fixation promotes a decrease in MRI relaxometry (T1 and T2), a decrease in myelin water fraction (MWF) measurements but accounting for minimal changes in diffusion tensor imaging (DTI) parameters such FA and mean diffusivity, (MD) (Shatil et al., 2018). Specifically, to mouse brain DTI and tractography studies, there is some change in the scalar metrics at one year after fixation, these changes are sufficiently small, particularly in WM to support reproducible connectomes over a period ranging from two weeks to one-year post-fixation (Xiao et al., 2020).

Also, it is a well-recognized fact that formalin fixation alters water diffusion coefficients in the context of pathological conditions, such as the infarcted brain (Sun et al., 2005) as well as in DTI preclinical studies with fresh ex vivo and fixed brains tissue (D'Arceuil et al., 2007) which has to be accounted for in the ex vivo pipeline of high-quality images (Dyrby et al., 2011) to improve the validation strategies for the interpretation of microstructure (Dyrby et al., 2018). In particular to our study, the chosen lower b-value (1000 s/mm^2) to acquire in our ex vivo study has been used in previous preclinical studies (Crombe et al., 2018; Wang et al., 2019). However, it is also probable that this particular lower b value maybe not enough (for the NODDI model) to completely distinguish the restricted diffusion for the intra-neurite compartment from other compartments, and a lower initial b value might be needed (Colon-Perez et al., 2019) and implemented in our future studies.

In terms of the initial diffusion parameters considered for the NODDI model, previous clinical studies explored the neurite compartment, setting the intrinsic parallel diffusivity d// to 1.7 μm^2 ms^{-1} evaluating the residuals concerning the parallel diffusivity in a range from 0.5 to 3.0 μm^2 ·ms^{-1} over tissue type and age (Guerrero et al., 2019). Interestingly, that study showed the optimum parallel diffusivity is significantly lower for GM relative to WM, and a significantly decreased in optimum parallel diffusivity in GM & WM in the infant group. Moreover, in recent clinical studies, researchers have optimized the value of d// for the cerebral cortex to 1.1×10^{-3} mm^2/s (from the default value of 1.7×10^{-3} mm^2/s) in the study of GM regions (Fukutomi et al., 2019). Although our studies used an

empirical diffusivity value equal for GM and WM brain structures, further studies are necessary to define specific GM diffusivity values in murine brain tissues.

Conceptual limitations of the dMRI models must be always considered due to the complexity of the biological materials under analysis. Different mechanisms can compensate for one another and lead to misinterpretations of the underlying events. As an example, immune cell infiltration, which results in a decrease in the apparent diffusion coefficient (ADC) (Sevick et al., 1992), can be counteracted by the vasogenic edema induced by neuroinflammation (Schlaug et al., 1997). Thus, the use of DTI derived parameters may not be specific enough to selectively quantify restricted diffusion in inflammatory tissues, where several interrelated cellular events are taking place simultaneously (Glass et al., 2010; Komine and Yamanaka, 2015; Ransohoff et al., 2015; Sochocka et al., 2017). FA could potentially fall short in the GM assessment due to its isotropic nature and particularly important in the short distance exchange of information. Thus, it is possible that the collection of cell bodies and apical dendrites are not represented by most of the isotropic features (Gatto, R. G. et al., 2020). Therefore, the use of more complex models ~~multi-compartmental~~ as non-Gaussian diffusion models, can improve our quantitative approach and interpretation of the microstructural events in preclinical models of HD (Gatto et al., 2015) and other NDDs (Gatto, 2020a; Gatto et al., 2019).

Even though DWI methods might be not specific to reflect all the biological changes occurring in HD, these methods can be influenced by axonal pathology as well as changes in myelin content, and advanced DWI models appear to improve correlations with histology (Albrecht et al., 2016). More and more aspects of neuroinflammation become accessible to probing by MRI/MRS, and an increasing number of studies are carried out taking advantage of the complementarity of the information provided by this technique (Quarantelli, 2015). The structural metrics obtained with these techniques are not direct measures of cell number or density and are likely to reflect a combination of many cellular processes. Nonetheless, these methods are sensitive to anatomical changes that can

occur in the context of pathology such as atrophy, which has been linked to inflammation. MRI metrics are important for the characterization of neuroinflammatory disorders, and some have already proven their usefulness for diagnosis, and follow-up of patients affected by neuroinflammation. (Albrecht et al., 2016). Advanced diffusion models, based on neurite orientation dispersion and density imaging (NODDI) in MR, have been proved to be sensitive to microglial density and the cellular changes associated with microglial activation in a preclinical setting (Yi et al., 2019). Astrocytes, the most abundant cell type in the brain, (Miller, 2018) show changes in neuroinflammation, but evidence derived by MRI on astrocytic activation are still confined to few groups, and often on limited samples (Cavaliere et al., 2020).

Overall, UHFD-MRI is an exceptional tool to study structural neurodegenerative features in preclinical HD models (Gatto et al., 2018a) (Weissmann et al., 2020) **(Fig. 12)**. However, the link between multiple macrostructural, microstructural, and neurochemical events are complex and still not well-understood. Thus, our approach encourages the combination of multiple dMRI models and analytical histological methods. Hence, this holistic approach improves the timing of potential therapeutic approaches.

CONCLUSIONS

Diffusion MRI can be used to extract information on early neuropathological events in a preclinical model of HD. Using a multiple dMRI technique approach, it is possible to non-invasively evaluate microstructural changes at early stages in different brain tissue compartments. Taken together, our studies showed that parameters from dMRI techniques, such as DTI and NODDI and complex histological analysis and lead to a better understanding of the disease. This study highlights the potential of UHFD-MRI to find early bioimaging markers, and use them to examine patients affected by HD.

CREDIT AUTHOR STATEMENT

All authors had full access to all the data in the study and take responsibility for the integrity of the data and the accuracy of the data analysis. RG conceptualized and visualized the experiments. RG, CW, and MA collected the data, conducted the experiments, and analyzed the MRI and histological data. MA and DD assisted with the MRI data collection and curation. JS provided the biological samples for these studies. QA, LG, and LCSC processed the mouse brains. CW conducted the histological studies. RG and CW analyzed and curated the data. RG and CW wrote the manuscript. OU, TM, and RM added their opinions and validated the manuscript.

5. ACKNOWLEDGMENTS

This study was supported by the High Magnetic Field Laboratory (NHMFL) and Advanced Magnetic Resonance Imaging and Spectroscopy (AMRIS) under Magnetic Laboratory Visiting Scientist Program (Award VSP #327) to RG. We would like to acknowledge Dr. James Collins (AMRIS) for his technical assistance with dMRI experiments. We thank Dr. Amaicha Deipino for providing us with the GFAP antibody, and Dr. Graciela Mazzone for the Iba1 antibody. Special thanks go to Darius Forghani for his help in logistics related to this project. The McKnight Brain Institute at the National High Magnetic Field Laboratory's AMRIS Facility is supported by the National Science Foundation (NSF) Cooperative Agreement No. DMR-1157490 and the State of Florida.

6. CONFLICT OF INTEREST STATEMENT

The authors certify that they have no affiliations with or involvement in any organization or entity that may have had any financial or nonfinancial interest in the subject matter.

7. ROLE OF AUTHORS

All authors had full access to all the data in the study and take responsibility for the integrity of the data and the accuracy of the data analysis. RG conceptualized and visualized the experiments. RG, CW, and collected the data, conducted the experiments, and analyzed the MRI and histological data. MA and DD assisted with the MRI data collection and curation. JS provided the biological samples for these studies. QA, LG, and LCSC processed the

mouse brains. CW conducted the histological studies. RG and CW analyzed and curated the data. RG and CW wrote the manuscript. OU, TM, and RM added their opinions and validated the manuscript.

8. DATA ACCESSIBILITY

The datasets generated and/or analyzed during the current study are available from either of the corresponding authors on reasonable request.

REFERENCES

Albrecht, D.S., Granziera, C., Hooker, J.M., Loggia, M.L., 2016. In Vivo Imaging of Human Neuroinflammation. ACS chemical neuroscience 7(4), 470-483.

Andersson, J.L., Skare, S., Ashburner, J., 2003. How to correct susceptibility distortions in spin-echo echo-planar images: application to diffusion tensor imaging. NeuroImage 20(2), 870-888.

Andersson, J.L.R., Sotiropoulos, S.N., 2016. An integrated approach to correction for off-resonance effects and subject movement in diffusion MR imaging. NeuroImage 125, 1063-1078.

Beery, A.K., 2018. Inclusion of females does not increase variability in rodent research studies. Curr Opin Behav Sci 23, 143-149.

Begeti, F., Schwab, L.C., Mason, S.L., Barker, R.A., 2016. Hippocampal dysfunction defines disease onset in Huntington's disease. Journal of neurology, neurosurgery, and psychiatry 87(9), 975-981.

Benjamini, Y., 2010. Discovering the false discovery rate. Journal of the Royal Statistical Society: Series B (Statistical Methodology) 72(4), 405-416.

Benjamini, Y., Hochberg, Y., 1995. Controlling the False Discovery Rate: A Practical and Powerful Approach to Multiple Testing. Journal of the Royal Statistical Society: Series B (Methodological) 57(1), 289-300.

Bondan, E.F., Cardoso, C.V., Martins, M.F.M., Otton, R., 2019. Memory impairments and increased GFAP expression in hippocampal astrocytes following hypercaloric diet in rats. Arquivos de neuro-psiquiatria 77(9), 601-608.

Bradford, J., Shin, J.Y., Roberts, M., Wang, C.E., Sheng, G., Li, S., Li, X.J., 2010. Mutant huntingtin in glial cells exacerbates neurological symptoms of Huntington disease mice. J Biol Chem 285(14), 10653-10661.

Castellanos, L.C.S., Rozenfeld, P., Gatto, R.G., Reisin, R.C., Uchitel, O.D., Weissmann, C., 2020. Upregulation of ASIC1a channels in an in vitro model of Fabry disease. Neurochem Int 140, 104824.

Cavaliere, C., Tramontano, L., Fiorenza, D., Alfano, V., Aiello, M., Salvatore, M., 2020. Gliosis and Neurodegenerative Diseases: The Role of PET and MR Imaging. Frontiers in cellular neuroscience 14(75), 75.

Cepeda-Prado, E., Popp, S., Khan, U., Stefanov, D., Rodriguez, J., Menalled, L.B., Dow-Edwards, D., Small, S.A., Moreno, H., 2012. R6/2 Huntington's disease mice develop early and progressive abnormal brain metabolism and seizures. The Journal of neuroscience : the official journal of the Society for Neuroscience 32(19), 6456-6467.

Chang, W.T., Puspitasari, F., Garcia-Miralles, M., Yeow, L.Y., Tay, H.C., Koh, K.B., Tan, L.J., Pouladi, M.A., Chuang, K.H., 2018. Connectomic imaging reveals Huntington-related pathological and pharmaceutical effects in a mouse model. NMR Biomed 31(12), e4007.

Charan, J., Kantharia, N.D., 2013. How to calculate sample size in animal studies? Journal of pharmacology & pharmacotherapeutics 4(4), 303-306.

Cisbani, G., Cicchetti, F., 2012. An in vitro perspective on the molecular mechanisms underlying mutant huntingtin protein toxicity. Cell death & disease 3, e382.

Collins, T.J., 2007. ImageJ for microscopy. Biotechniques 43(1 Suppl), 25-30.

Colon-Perez, L.M., Ibanez, K.R., Suarez, M., Torroella, K., Acuna, K., Ofori, E., Levites, Y., Vaillancourt, D.E., Golde, T.E., Chakrabarty, P., Febo, M., 2019. Neurite orientation dispersion and density imaging reveals white matter and hippocampal microstructure changes produced by Interleukin-6 in the TgCRND8 mouse model of amyloidosis. NeuroImage 202, 116138.

Cowan, C.M., Raymond, L.A., 2006. Selective neuronal degeneration in Huntington's disease. Current topics in developmental biology 75, 25-71.

Crombe, A., Planche, V., Raffard, G., Bourel, J., Dubourdieu, N., Panatier, A., Fukutomi, H., Dousset, V., Oliet, S., Hiba, B., Tourdias, T., 2018. Deciphering the microstructure of hippocampal subfields with in vivo DTI and NODDI: Applications to experimental multiple sclerosis. NeuroImage 172, 357-368.

D'Arceuil, H.E., Westmoreland, S., de Crespigny, A.J., 2007. An approach to high resolution diffusion tensor imaging in fixed primate brain. NeuroImage 35(2), 553-565.

Daly, J., Cohen, J., 1987. Statistical Power Analysis For The Behavioral Sciences Revised Edition.

Dattalo, P., 2018. Determining Sample Size Using Fast and Slow Thinking. Journal of Social Service Research 44(2), 180-190.

Dhital, B., Kellner, E., Kiselev, V.G., Reisert, M., 2018. The absence of restricted water pool in brain white matter. NeuroImage 182, 398-406.

Di Leva, A., 2016. The fractal geometry of the brain.

Douaud, G., Behrens, T.E., Poupon, C., Cointepas, Y., Jbabdi, S., Gaura, V., Golestani, N., Krystkowiak, P., Verny, C., Damier, P., Bachoud-Levi, A.C., Hantraye, P., Remy, P., 2009. In vivo evidence for the selective subcortical degeneration in Huntington's disease. NeuroImage 46(4), 958-966.

Dyrby, T.B., Baare, W.F., Alexander, D.C., Jelsing, J., Garde, E., Sogaard, L.V., 2011. An ex vivo imaging pipeline for producing high-quality and high-resolution diffusion-weighted imaging datasets. Human brain mapping 32(4), 544-563.

Dyrby, T.B., Innocenti, G.M., Bech, M., Lundell, H., 2018. Validation strategies for the interpretation of microstructure imaging using diffusion MRI. NeuroImage 182, 62-79.

Fazio, P., Paucar, M., Svenningsson, P., Varrone, A., 2018. Novel Imaging Biomarkers for Huntington's Disease and Other Hereditary Choreas. Current neurology and neuroscience reports 18(12), 85.

Ferrante, R.J., 2009. Mouse models of Huntington's disease and methodological considerations for therapeutic trials. Biochim Biophys Acta 1792(6), 506-520.

Figiel, M., Szlachcic, W.J., Switonski, P.M., Gabka, A., Krzyzosiak, W.J., 2012. Mouse models of polyglutamine diseases: review and data table. Part I. Mol Neurobiol 46(2), 393-429.

Finkbeiner, S., 2011. Huntington's Disease. Cold Spring Harbor perspectives in biology 3(6).

Fukutomi, H., Glasser, M.F., Murata, K., Akasaka, T., Fujimoto, K., Yamamoto, T., Autio, J.A., Okada, T., Togashi, K., Zhang, H., Van Essen, D.C., Hayashi, T., 2019. Diffusion Tensor Model links to Neurite Orientation Dispersion and Density Imaging at high b-value in Cerebral Cortical Gray Matter. Scientific reports 9(1), 12246.

Gatto, R.G., 2020a. Editorial for "Evaluating the Therapeutic Effect of Low-Intensity Transcranial Ultrasound on Traumatic Brain Injury With Diffusion Kurtosis Imaging". Journal of magnetic resonance imaging: JMRI 52(2), 532-533.

Gatto, R.G., 2020b. Molecular and microstructural biomarkers of neuroplasticity in neurodegenerative disorders through preclinical and diffusion magnetic resonance imaging studies. Journal of integrative neuroscience 19(3), 571-592.

Gatto, R.G., Amin, M.Y., Deyoung, D., Hey, M., Mareci, T.H., Magin, R.L., 2018a. Ultra-High Field Diffusion MRI Reveals Early Axonal Pathology in Spinal Cord of ALS mice. Translational neurodegeneration 7, 20.

Gatto, R.G., Chu, Y., Ye, A.Q., Price, S.D., Tavassoli, E., Buenaventura, A., Brady, S.T., Magin, R.L., Kordower, J.H., Morfini, G.A., 2015. Analysis of YFP(J16)-R6/2 reporter mice and postmortem brains reveals early pathology and increased vulnerability of callosal axons in Huntington's disease. Hum Mol Genet 24(18), 5285-5298.

Gatto, R.G., Li, W., Gao, J., Magin, R.L., 2018b. In vivo diffusion MRI detects early spinal cord axonal pathology in a mouse model of amyotrophic lateral sclerosis. NMR Biomed 31(8), e3954.

Gatto, R.G., Mustafi, S.M., Amin, M.Y., Mareci, T.H., Wu, Y.C., Magin, R.L., 2018c. Neurite orientation dispersion and density imaging can detect presymptomatic axonal degeneration in the spinal cord of ALS mice. Functional neurology 33(3), 155-163.

Gatto, R.G., Weissmann, C., 2019. Diffusion Tensor Imaging in Preclinical and Human Studies of Huntington's Disease: What Have we Learned so Far? Curr Med Imaging Rev 15(6), 521-542.

Gatto, R.G., Weissmann, C., Amin, M., Finkielsztein, A., Sumagin, R., Mareci, T.H., Uchitel, O.D., Magin, R.L., 2020. Assessing neuraxial microstructural changes in a transgenic mouse model of early-stage Amyotrophic Lateral Sclerosis by ultra-high field MRI and diffusion tensor metrics. Animal models and experimental medicine 3(2), 117-129.

Gatto, R.G., Ye, A.Q., Colon-Perez, L., Mareci, T.H., Lysakowski, A., Price, S.D., Brady, S.T., Karaman, M., Morfini, G., Magin, R.L., 2019. Detection of axonal degeneration in a mouse model of Huntington's disease: comparison between diffusion tensor imaging and anomalous diffusion metrics. Magma 32(4), 461-471.

Glass, C.K., Saijo, K., Winner, B., Marchetto, M.C., Gage, F.H., 2010. Mechanisms underlying inflammation in neurodegeneration. Cell 140(6), 918-934.

Guerrero, J.M., Adluru, N., Bendlin, B.B., Goldsmith, H.H., Schaefer, S.M., Davidson, R.J., Kecskemeti, S.R., Zhang, H., Alexander, A.L., 2019. Optimizing the intrinsic parallel diffusivity in NODDI: An extensive empirical evaluation. PloS one 14(9), e0217118.

Gupta, R.K., Nath, K., Prasad, A., Prasad, K.N., Husain, M., Rathore, R.K., Husain, N., Srivastava, C., Khetan, P., Trivedi, R., Narayana, P.A., 2008. In vivo demonstration of neuroinflammatory molecule expression in brain abscess with diffusion tensor imaging. AJNR. American journal of neuroradiology 29(2), 326-332.

Gupta, R.K., Srivastava, S., Saksena, S., Rathore, R.K., Awasthi, R., Prasad, K.N., Husain, M., Pandey, C.M., Husain, N., 2010. Correlation of DTI metrics in the wall and cavity of brain abscess with histology and immunohistochemistry. NMR Biomed 23(3), 262-269.

Gupta, R.K., Trivedi, R., Awasthi, R., Paliwal, V.K., Prasad, K.N., Rathore, R.K., 2012. Understanding changes in DTI metrics in patients with different stages of neurocysticercosis. Magn Reson Imaging 30(1), 104-111.

Halliday, G., Herrero, M.T., Murphy, K., McCann, H., Ros-Bernal, F., Barcia, C., Mori, H., Blesa, F.J., Obeso, J.A., 2009. No Lewy pathology in monkeys with over 10 years of severe MPTP Parkinsonism. Movement disorders : official journal of the Movement Disorder Society 24(10), 1519-1523.

Hansson, O., Petersén, Å., Leist, M., Nicotera, P., Castilho, R.F., Brundin, P., 1999. Transgenic mice expressing a Huntington's disease mutation are resistant to quinolinic acid-induced striatal excitotoxicity. PNAS 96(15), 8727-8732.

Harris, K.L., Armstrong, M., Swain, R., Erzinclioglu, S., Das, T., Burgess, N., Barker, R.A., Mason, S.L., 2019. Huntington's disease patients display progressive deficits in hippocampal-dependent cognition during a task of spatial memory. Cortex; a journal devoted to the study of the nervous system and behavior 119, 417-427.

Heikkinen, T., Lehtimaki, K., Vartiainen, N., Puolivali, J., Hendricks, S.J., Glaser, J.R., Bradaia, A., Wadel, K., Touller, C., Kontkanen, O., Yrjanheikki, J.M., Buisson, B., Howland, D., Beaumont, V., Munoz-Sanjuan, I., Park, L.C., 2012. Characterization of neurophysiological and behavioral changes, MRI brain volumetry and 1H MRS in zQ175 knock-in mouse model of Huntington's disease. PloS one 7(12), e50717.

Hobbs, N.Z., Barnes, J., Frost, C., Henley, S.M., Wild, E.J., Macdonald, K., Barker, R.A., Scahill, R.I., Fox, N.C., Tabrizi, S.J., 2010. Onset and progression of pathologic atrophy in Huntington disease: a longitudinal MR imaging study. AJNR. American journal of neuroradiology 31(6), 1036-1041.

Holz, M., Heil, S.R., Sacco, A., 2000. Temperature-dependent self-diffusion coefficients of water and six selected molecular liquids for calibration in accurate 1H NMR PFG measurements. Physical Chemistry Chemical Physics 2(20), 4740-4742.

Jenkinson, M., Beckmann, C.F., Behrens, T.E., Woolrich, M.W., Smith, S.M., 2012. Fsl. NeuroImage 62(2), 782-790.

Kamiya, K., Hori, M., Aoki, S., 2020. NODDI in clinical research. Journal of neuroscience methods 346, 108908.

Kapitulnik, A., Deutscher, G., 1984. Percolation scale effects in metal-insulator thin films. Journal of Statistical Physics 36(5-6), 815-826.

Komine, O., Yamanaka, K., 2015. Neuroinflammation in motor neuron disease. Nagoya journal of medical science 77(4), 537-549.

Li, J.Y., Popovic, N., Brundin, P., 2005. The use of the R6 transgenic mouse models of Huntington's disease in attempts to develop novel therapeutic strategies. NeuroRx 2(3), 447-464.

Magnotta, V.A., Kim, J., Koscik, T., Beglinger, L.J., Espinso, D., Langbehn, D., Nopoulos, P., Paulsen, J.S., 2009. Diffusion Tensor Imaging in Preclinical Huntington's Disease. Brain imaging and behavior 3(1), 77-84.

Mancini, A., Gaetani, L., Di Gregorio, M., Tozzi, A., Ghiglieri, V., Calabresi, P., Di Filippo, M., 2017. Hippocampal neuroplasticity and inflammation: relevance for multiple sclerosis. Multiple Sclerosis and Demyelinating Disorders 2(1), 2.

Miller, S.J., 2018. Astrocyte Heterogeneity in the Adult Central Nervous System. Frontiers in cellular neuroscience 12(401), 401.

Muller, H.P., Roselli, F., Rasche, V., Kassubek, J., 2020. Diffusion Tensor Imaging-Based Studies at the Group-Level Applied to Animal Models of Neurodegenerative Diseases. Front Neurosci 14, 734.

Naver, B., Stub, C., Moller, M., Fenger, K., Hansen, A.K., Hasholt, L., Sorensen, S.A., 2003. Molecular and behavioral analysis of the R6/1 Huntington's disease transgenic mouse. Neuroscience 122(4), 1049-1057.

Palpagama, T.H., Waldvogel, H.J., Faull, R.L.M., Kwakowsky, A., 2019. The Role of Microglia and Astrocytes in Huntington's Disease. Frontiers in molecular neuroscience 12(258), 258.

Paxinos, G., Franklin, K.B.J., 2004. The mouse brain in stereotaxic coordinates, Compact 2nd ed. Elsevier Academic Press, Amsterdam ; Boston.

Phillips, O., Sanchez-Castaneda, C., Elifani, F., Maglione, V., Di Pardo, A., Caltagirone, C., Squitieri, F., Sabatini, U., Di Paola, M., 2013. Tractography of the corpus callosum in Huntington's disease. PloS one 8(9), e73280.

Phillips, O., Squitieri, F., Sanchez-Castaneda, C., Elifani, F., Caltagirone, C., Sabatini, U., Di Paola, M., 2014. Deep white matter in Huntington's disease. PloS one 9(10), e109676.

Pirici, D., Mogoanta, L., Margaritescu, O., Pirici, I., Tudorica, V., Coconu, M., 2009. Fractal analysis of astrocytes in stroke and dementia. Romanian journal of morphology and embryology = Revue roumaine de morphologie et embryologie 50(3), 381-390.

Politis, M., Lahiri, N., Niccolini, F., Su, P., Wu, K., Giannetti, P., Scahill, R.I., Turkheimer, F.E., Tabrizi, S.J., Piccini, P., 2015. Increased central microglial activation associated with peripheral cytokine levels in premanifest Huntington's disease gene carriers. Neurobiology of disease 83, 115-121.

Quarantelli, M., 2015. MRI/MRS in neuroinflammation: methodology and applications. Clinical and translational imaging 3(6), 475-489.

Quirion, J.G., Parsons, M.P., 2019. The Onset and Progression of Hippocampal Synaptic Plasticity Deficits in the Q175FDN Mouse Model of Huntington Disease. Frontiers in cellular neuroscience 13, 326.

Ransohoff, R.M., Schafer, D., Vincent, A., Blachere, N.E., Bar-Or, A., 2015. Neuroinflammation: Ways in Which the Immune System Affects the Brain. Neurotherapeutics : the journal of the American Society for Experimental NeuroTherapeutics 12(4), 896-909.

Rattray, I., Smith, E.J., Crum, W.R., Walker, T.A., Gale, R., Bates, G.P., Modo, M., 2013. Correlations of behavioral deficits with brain pathology assessed through longitudinal MRI and histopathology in the R6/1 mouse model of Huntington's disease. PloS one 8(12), e84726.

Reichenbach, A., Siegel, A., Senitz, D., Smith, T.G., 1992. A comparative fractal analysis of various mammalian astroglial cell types. NeuroImage 1(1), 69-77.

Rosas, H.D., Tuch, D.S., Hevelone, N.D., Zaleta, A.K., Vangel, M., Hersch, S.M., Salat, D.H., 2006. Diffusion tensor imaging in presymptomatic and early Huntington's disease: Selective white matter pathology and its relationship to clinical measures. Movement disorders : official journal of the Movement Disorder Society 21(9), 1317-1325.

Rosenthal, R., Rosnow, R.L., 1984. Essentials of Behavioral Research: Methods and Data Analysis.

Roze, E., Bonnet, C., Betuing, S., Caboche, J., 2010. Huntington's disease. Advances in experimental medicine and biology 685, 45-63.

Ruocco, H.H., Lopes-Cendes, I., Li, L.M., Santos-Silva, M., Cendes, F., 2006. Striatal and extrastriatal atrophy in Huntington's disease and its relationship with length of the CAG repeat. Braz J Med Biol Res 39(8), 1129-1136.

Schilling, K.G., Yeh, F.C., Nath, V., Hansen, C., Williams, O., Resnick, S., Anderson, A.W., Landman, B.A., 2019. A fiber coherence index for quality control of B-table orientation in diffusion MRI scans. Magn Reson Imaging 58, 82-89.

Schlaug, G., Siewert, B., Benfield, A., Edelman, R.R., Warach, S., 1997. Time course of the apparent diffusion coefficient (ADC) abnormality in human stroke. Neurology 49(1), 113-119.

Schneider, C.A., Rasband, W.S., Eliceiri, K.W., 2012. NIH Image to ImageJ: 25 years of image analysis. Nature methods 9(7), 671-675.

Segovia, J., 2002. Transgenic Model for the Study of Oxidative Damage in Huntington's Disease, in Sen, C.K., Packer, L. (Eds.), Redox Cell Biology and Genetics Part B. Academic Press, pp. 365-373.

Sevick, R.J., Kanda, F., Mintorovitch, J., Arieff, A.I., Kucharczyk, J., Tsuruda, J.S., Norman, D., Moseley, M.E., 1992. Cytotoxic brain edema: assessment with diffusion-weighted MR imaging. Radiology 185(3), 687-690.

Shatil, A.S., Uddin, M.N., Matsuda, K.M., Figley, C.R., 2018. Quantitative Ex Vivo MRI Changes due to Progressive Formalin Fixation in Whole Human Brain Specimens: Longitudinal Characterization of Diffusion, Relaxometry, and Myelin Water Fraction Measurements at 3T. Front Med (Lausanne) 5, 31.

Shim, J.H., Im, S.J., Kim, A.Y., Kim, Y.T., Kim, E.B., Baek, H.M., 2019. Generation of Mouse Basal Ganglia Diffusion Tractography Using 9.4T MRI. Experimental neurobiology 28(2), 300-310.

Shin, J.Y., Fang, Z.H., Yu, Z.X., Wang, C.E., Li, S.H., Li, X.J., 2005. Expression of mutant huntingtin in glial cells contributes to neuronal excitotoxicity. J Cell Biol 171(6), 1001-1012.

Sieradzan, K.A., Mann, D.M., 2001. The selective vulnerability of nerve cells in Huntington's disease. Neuropathol Appl Neurobiol 27(1), 1-21.

Sochocka, M., Diniz, B.S., Leszek, J., 2017. Inflammatory Response in the CNS: Friend or Foe? Mol Neurobiol 54(10), 8071-8089.

Steventon, J.J., Trueman, R.C., Ma, D., Yhnell, E., Bayram-Weston, Z., Modat, M., Cardoso, J., Ourselin, S., Lythgoe, M., Stewart, A., Rosser, A.E., Jones, D.K., 2016. Longitudinal in vivo MRI in a Huntington's disease mouse model: Global atrophy in the absence of white matter microstructural damage. Scientific reports 6, 32423.

Sun, S.W., Neil, J.J., Liang, H.F., He, Y.Y., Schmidt, R.E., Hsu, C.Y., Song, S.K., 2005. Formalin fixation alters water diffusion coefficient magnitude but not anisotropy in infarcted brain. Magn Reson Med 53(6), 1447-1451.

Switonski, P.M., Szlachcic, W.J., Gabka, A., Krzyzosiak, W.J., Figiel, M., 2012. Mouse models of polyglutamine diseases in therapeutic approaches: review and data table. Part II. Mol Neurobiol 46(2), 430-466.

Ugolini, F., Lana, D., Nardiello, P., Nosi, D., Pantano, D., Casamenti, F., Giovannini, M.G., 2018. Different Patterns of Neurodegeneration and Glia Activation in CA1 and CA3 Hippocampal Regions of TgCRND8 Mice. Frontiers in aging neuroscience 10(372), 372.

Vonsattel, J.P., Myers, R.H., Stevens, T.J., Ferrante, R.J., Bird, E.D., Richardson, E.P., Jr., 1985. Neuropathological classification of Huntington's disease. J Neuropathol Exp Neurol 44(6), 559-577.

Vorisek, I., Syka, M., Vargova, L., 2017. Brain Diffusivity and Structural Changes in the R6/2 Mouse Model of Huntington Disease. J Neurosci Res 95(7), 1474-1484.

Walker, F.O., 2007. Huntington's disease. Lancet 369(9557), 218-228.

Wang, N., Zhang, J., Cofer, G., Qi, Y., Anderson, R.J., White, L.E., Allan Johnson, G., 2019. Neurite orientation dispersion and density imaging of mouse brain microstructure. Brain structure & function 224(5), 1797-1813.

Weissmann, C., Amin, M., Angeles-López, A.D., García-Lara, L., Salinas Castellanos, L.C., Deyoung, D., Segovia, J., Mareci, T.H., Uchitel, O.D., Magin, R.L., Gatto, R.G., 2020. Early Changes in Structural Brain Bioimaging Markers from an R6/1 Mouse Model of Huntington's Disease Captured by Ultra-High Field MRI, Biomarkers of Paris (BMP). Paris (Virtual).

Xiang, Z., Valenza, M., Cui, L., Leoni, V., Jeong, H.K., Brilli, E., Zhang, J., Peng, Q., Duan, W., Reeves, S.A., Cattaneo, E., Krainc, D., 2011. Peroxisome-proliferator-activated receptor gamma coactivator 1 alpha contributes to dysmyelination in experimental models of Huntington's disease. The Journal of neuroscience : the official journal of the Society for Neuroscience 31(26), 9544-9553.

Xiao, J., Hornburg, K.J., Cofer, G., Cook, J.J., Qi, Y., Johnson, G.A., 2020. A time-course study of actively stained mouse brains: DTI parameter and connectomic stability over one year. 2020.2012.2002.407338.

Yeh, F.C., Verstynen, T.D., Wang, Y., Fernandez-Miranda, J.C., Tseng, W.Y., 2013. Deterministic diffusion fiber tracking improved by quantitative anisotropy. PloS one 8(11), e80713.

Yi, S.Y., Barnett, B.R., Torres-Velazquez, M., Zhang, Y., Hurley, S.A., Rowley, P.A., Hernando, D., Yu, J.J., 2019. Detecting Microglial Density With Quantitative Multi-Compartment Diffusion MRI. Front Neurosci 13(81), 81.

Young, K., Morrison, H., 2018. Quantifying Microglia Morphology from Photomicrographs of Immunohistochemistry Prepared Tissue Using ImageJ. Journal of visualized experiments: JoVE(136).

Yushkevich, P.A., Piven, J., Hazlett, H.C., Smith, R.G., Ho, S., Gee, J.C., Gerig, G., 2006. User-guided 3D active contour segmentation of anatomical structures: significantly improved efficiency and reliability. NeuroImage 31(3), 1116-1128.

Yushkevich, P.A., Yang, G., Gerig, G., 2016. ITK-SNAP: An interactive tool for semi-automatic segmentation of multi-modality biomedical images. Annu Int Conf IEEE Eng Med Biol Soc 2016, 3342-3345.

Zhang, H., Schneider, T., Wheeler-Kingshott, C.A., Alexander, D.C., 2012. NODDI: practical in vivo neurite orientation dispersion and density imaging of the human brain. NeuroImage 61(4), 1000-1016.

Zheng, Z., Diamond, M.I., 2012. Huntington's disease and the huntingtin protein. Prog Mol Biol Transl Sci 107, 189-214.

Table 1 - *DTI parameters from brain ROIs in the R6/1 mice.* **Abbreviations**: WT, wild type; R6/1, transgenic mouse model of HD; wks, weeks; FrA, frontal accessory area; CCX, cortex; Cing, cingulate cortical area; M1, primary motor area; M2, secondary motor area, CC, corpus callosum; STR, striatum, HC hippocampus; DTI, diffusion tensor imaging, FA, fractional anisotropy; AD, axial diffusivity; RD, radial diffusivity; MD, mean diffusivity. (# = $p<0.05$, # # = $p<0.01$, # # # = $p<0.001$).

Table 2 - *NODDI outputs from ROIs in the R6/1 mice.* **Abbreviations**: HD, Huntington's disease; WT, wild type; R6/1, a transgenic mouse model of HD; FrA, frontal accessory area; CCX, cortex; Cing, cingulate cortical area;

M1, primary motor area; M2, secondary motor area, CC, corpus callosum; STR, striatum, HC hippocampus; NODDI, neurite orientation dispersion and density Imaging; ICVF; intracellular volume fraction; ODI; orientation dispersion index; ISO; isotropic volume fraction.

Table 3 - *Previous diffusion MRI studies in the R6 mice*. **Abbreviations:** DTI, diffusion tensor imaging; CTWR, continuous random walk model; WM, white matter; GM, grey matter; T, Tesla; dir, gradient direction; FA fractional anisotropy; AD, axial diffusivity; RD; radial diffusivity; MD; mean diffusivity; α, complexity coefficient; ADCW, apparent diffusion coefficient of Water; wks., weeks; P, post-natal day; cc. corpus callosum; CCX, cortex; pal, pallidum; ↑, increased compared to WT; ↓, decreased compared to WT.

Table 1 - DTI outputs from segmented R6/1 mice regions.

Brain Structure	**FA** †				**AD** (10^{-4} mm/s^{-1}) *			**RD** (10^{-4} mm/s^{-1}) *			**MD** (10^{-4} mm/s^{-1}) *		
	WT (11wks)	R6/1 (11wks)	WT (**30**wks)	R6/1 (30wks)	WT (11wks)	R6/1 (11wks)	R6/1 (30wks)	WT (11wks)	R6/1 (11wks)	R6/1 (30wks)	WT (11wks)	R6/1 (11wks)	R6/1 (30wks)
CC (Genu)	0.59 ± 0.01	0.51 ± 0.01 ▼14% (##)	0.58 ± 0.01	0.45 ± 0.01 ▼22% (###)	4.61 ± 0.02	5.46 ± 0.002 ▲18 % (##)	5.85 ± 0.01 ▲27 % (###)	2.94 ± 0.01	3.26 ± 0.01 ▲11% (#)	3.52 ± 0.01 ▲20 % (###)	2.01 ± 0.01	2.32 ± 0.002 ▲15 % (##)	2.95 ± 0.01 ▲47 % (###)
CC (Body)	0.56 ± 0.02	0.53 ± 0.02 ▼5%	0.56 ± 0.01	0.50 ± 0.03 ▼11% (#)	4.44 ± 0.01	4.46 ± 0.02 ▲<1 %	4.68 ± 0.03 ▲5%	3.01 ± 0.01	3.07 ± 0.02 ▲2%	3.41 ± 0.13 ▲13 % (##)	2.20 ± 0.01	2.28 ± 0.06 ▲4%	2.40 ± 0.13 ▲9% (#)
CC (Spleniu m)	0.57 ± 0.03	0.55 ± 0.03 ▼4%	0.53 ± 0.02	0.50 ± 0.06 ▼6%	4.68 ± 001	4.52 ± 0.02 ▲3%	4.98 ± 0,03 ▲6%	2.98 ± 0.11	3.19 ± 0.16 ▲7%	3.44 ± 0.54 ▲15 % (##)	2.21± 001	2.23 ± 0.01 ▲<1 %	2.45 ± 0,01 ▲11 % (##)
CCX (FrAc)	0.34 ± 0.01	0.26 ± 0.02 ▼24% (###)	0.31 ± 0.07	0.24 ± 0.01 ▼23% (###)	3.69 ± 0.01	4.18 ± 0.01 ▲13 % (##)	4.79 ± 0.02 ▲30 % (###)	2.85 ± 0.01	3.27±0 .01 ▲15% (##)	3.88 ± 0.02 ▲36 % (###)	2.47 ± 001	2.95 ± 0.01 ▲19 % (##)	3.10 ± 0,01 ▲26 % (###)
CCX (Cing)	0.35 ± 0.01	0.30 ± 0.01 ▼14% (##)	0.32 ± 0.06	0.28 ± 0.01 ▼13% (##)	4.36 ± 0.01	4.69 ± 0.01 ▲8% (#)	4.83 ± 0.02 ▲12 % (##)	3.32 ± 0.01	3.67 ± 0.01 ▲11% (###)	4.07 ± 0.02 ▲23 % (###)	2.36 ± 001	2.69 ± 0.01 ▲14 % (##)	3.18 ± 0,01 ▲35 % (###)
CCX (M2)	0.34 ± 0.01	0.30 ± 0.02 ▼12% (##)	0.33 ± 0.09	0.27 ± 0.01 ▼18% (##)	4.06 ± 0.01	4.37 ± 0.01 ▲8% (#)	5.13 ± 0.02 ▲26 % (###)	3.02 ± 0.01	3.36 ± 0.01 ▲11% (##)	3.83 ± 0.01 ▲27 % (###)	2.48 ± 001	2.86 ± 0.01 ▲15 % (##)	3.19 ± 0,01 ▲29 % (###)
CCX (M1)	0.34 ± 0.01	0.30 ± 0.01 ▼12% (##)	0.32 ± 0.06	0.26 ± 0.01 ▼19% (##)	3.88 ± 0.01	4.34 ± 0.01 ▲12 % (##)	4.95 ± 0.01 ▲28 % (###)	3.16 ± 0.01	3.40 ± 0.01 ▲8% (##)	3.86 ± 0.02 ▲22 % (###)	2.78 ± 001	3.19 ± 0.01 ▲15 % (##)	3.56 ± 0,01 ▲28 % (###)
HC	0.36 ± 0.01	0.31 ± 0.01 ▼14% (##)	0.34 ± 0.01	0.28 ± 0.01 ▼18% (##)	4.36 ± 0.02	4.76 ± 0.01 ▲9% (#)	5.18 ± 0.01 ▲19 % (###)	3.10 ± 0.02	3.57 ± 0.01 ▲15% (##)	3.71 ± 0.02 ▲20 % (###)	2.66 ± 001	3.08 ± 0.01 ▲16 % (##)	3.31 ± 0,01 ▲24 % (###)
STR	0.29 ± 0.01	0.42 ± 0.01 ▲45% (###)	0.31 ± 0.01	0.49 ± 0.02 ▲58% (###)	4.88 ± 0.01	4.51 ± 0.02 ▼13 % (##)	4..40 ± 0.01 ▼10 % (##)	3.69 ± 0.01	2.75 ± 0.01 ▼25% (##)	2.61 ± 0.01 ▼29 % (###)	3.09 ± 001	2.62 ± 0.01 ▼15 % (##)	2.44 ± 0,01 ▼21 % (###)

Abbreviations: WT, wild type; R6/1, a transgenic mouse model of HD; wks., weeks; FrA, frontal accessory area; CCX, cortex; Cing, cingulate cortical area; M1, primary motor area; M2, secondary motor area, CC, corpus callosum; Splen., splenium; STR, striatum, HC, hippocampus; DTI, diffusion tensor imaging, FA, fractional anisotropy; AD, axial diffusivity; RD, radial diffusivity; MD, mean diffusivity; ▲%, percentage of increase; ▼%, percentage of decrease. (# = p<0.05, # # = p<0.01, # # # = p<0.001), (n=4 per group). †R6/1 (11wks) and R6/1 (30wks) FA values are compared to their WT (11wks) and WT (30wks) respective controls. * R6/1 (11wks) and R6/1 (30wks) AD, RD, and MD values are compared to WT (11wks).

Table 2 - NODDI output variables from segmented R6/1 mice brain regions

Brain Structure	ICVF †				ODI †				IsoVF †			
	WT (11wks)	R6/1 (11wks)	WT (30wks)	R6/1 (30wks)	WT (11wks)	R6/1 (11wks)	WT (30wks)	R6/1 (30wks)	WT (11wks)	R6/1 (11wks)	WT (30wks)	R6/1 (30wks)
CC (Genu)	0.45 ± 0.01	0.38 ± 0.01 ▼16% (##)	0.44 ± 0.07	0.34 ± 0.01 ▼23% (###)	0.16 ± 0.01	0.19 ± 0.01 ▲19% (##)	0.17 ± 0.05	0.21 ± 0.01 ▲24% (###)	0.0096 ± 0.0025	0.0172 ± 0.0022 ▲79% (###)	0.0108 ± 0.0014	0.0212 ± 0.0043 ▲96% (###)
CC (Body)	0.48 ± 0.01	0.41 ± 0.01 ▼15% (##)	0.48 ± 0.01	0.42 ± 0.01 ▼13% (###)	0.29 ± 0.02	0.40 ± 0.01 ▲38% (###)	0.31 ± 0.02	0.42 ± 0.01 ▲35 % (###)	0.0031 ± 0.0015	0.0048 ± 0.0010 ▲55% (###)	0.0032 ± 0.0052	0.0067 ± 0.0013 ▲109% (###)
CC (Spleniu m)	0.48 ± 0.01	0.42 ± 0.01 ▼13% (#)	0.48 ± 0.01	0.40 ± 0.01 ▼18% (##)	0.15 ± 0.01	0.16 ± 0.01 ▲6%	0.18 ± 0.01	0.21 ± 0.01 ▲17 % (##)	0.0036 ± 0.0008	0.0041 ± 0.0010 ▲14% (#)	0.0038 ± 0.0024	0.0073 ± 0.0011 ▲92 % (###)
CCX (FrAc)	0.43 ± 0.01	0.36 ± 0.01 ▼16% (##)	0.41 ± 0.07	0.32 ± 0.02 ▼22% (###)	0.28 ± 0.01	0.40 ± 0.01 ▲43% (###)	0.36 ± 0.04	0.42 ± 0.02 ▲17 % (##)	0.0014 ± 0.0004	0.0059 ± 0.0019 ▲321 % (###)	0.0016 ± 0.0008	0.0081 ± 0.0019 ▲406% (###)
CCX (Cing)	0.40 ± 0.01	0.33 ± 0.01 ▼18% (##)	0.39 ± 0.05	0.29 ± 0.02 ▼26% (###)	0.29 ± 0.01	0.39 ± 0.01 ▲34 % (###)	0.30 ± 0.02	0.43 ± 0.01 ▲43 % (###)	0.0019 ± 0.0006	0.0062 ± 0.0018 ▲226 % (###)	0.0019 ± 0.0006	0.0078 ± 0.0021 ▲311% (###)
CCX (M2)	0.34 ± 0.01	0.32 ± 0.01 ▼6%	0.33 ± 0.05	0.25 ± 0.01 ▼24% (###)	0.27 ± 0.01	0.37 ± 0.01 ▲37% (###)	0.27 ± 0.01	0.35 ± 0.01 ▲30 %	0.0030 ± 0.0004	0.0037 ± 0.0007 ▲23%	0.0032 ± 0.006	0.0056 ± 0.0015

							(###)		(###)		▲75 % (###)
CCX (M1)	0.30 ± 0.01	0.27 ± 0.01 ▼10% (#)	0.32 ± 0.08	0.22 ± 0.01 ▼31% (###)	0.25 ± 0.01	0.34 ± 0.01 ▲36 % (###)	0.25 ± 0.01	0.35 ± 0.01 ▲40 % (###)	0.0035 ± 0.0003	0.0048 ± 0.0011 ▲37% (###)	0.0038 ± 0.0015	0.0051 ± 0.0012 ▲34 % (###)
HC	0.36 ± 0.01	0.30 ± 0.01 ▼17% (##)	0.36 ± 0.03	0.27 ± 0.01 ▼25% (###)	0.24 ± 0.01	0.27 ± 0.01 ▲13% (#)	0.25 ± 0.05	0.34 ± 0.01 ▲36 % (###)	0.0043 ± 0.0007	0.0118 ± 0.0019 ▲174 % (###)	0.0046 ± 0.0005	0.0081 ± 0.0012 ▲76 % (###)
STR	0.33 ± 0.01	0.38 ± 0.01 ▲15% (##)	0.33 ± 0.04	0.41 ± 0.01 ▲24% (###)	0.35 ± 0.01	0.29 ± 0.01 ▼17% (##)	0.34 ± 0.05	0.27 ± 0.02 ▼21 % (###)	0.0056 ± 0.0018	0.0129 ± 0.0025 ▲130 % (###)	0.0060 ± 0.0010	0.0197 ± 0.0041 ▲228% (###)

Abbreviations: WT, wild type; R6/1, a transgenic mouse model of Huntington's disease; CCX, cortex; FrA, frontal accessory area; Cing, cingulate cortical area; M1, primary motor area; M2, secondary motor area, CC, corpus callosum; STR, striatum, HC, hippocampus; NODDI, neurite orientation dispersion and density imaging; ICVF; intracellular volume fraction; ODI; orientation dispersion index; IsoVF; isotropic volume fraction.; ▲%, percentage of increase compared to the WT group; ▼%, percentage of decrease compared to the WT group. (# = p<0.05, # # = p<0.01, # # # = p<0.001), (n=4 per group). †Note that FA values from R6/1 (11wks) and R6/1 (30wks) are compared to their respective controls WT-11wks and WT-30wks.

Table 3 - Representative High-field MRI diffusion studies in R6 mice models of Huntington's disease.

Study/year (type)	Mouse model	Diffusion technique	Field strength	b value/s & gradient directions	Brain Structures Analyzed
Gatto et al 2019a (ex vivo) ***(Gatto et al., 2019)***	R6/2 (160CAG) M&F, P60 (n=3 per group)	DTI & CTRW	17.6T	b=1500 (s/mm²), 12dir & 400, 800, 1500, 3000, 5000, 7500, 10,000, 12,000, 15,000, 20,000 (s/mm²). 3dir	WM (CC genu)
Vorisek et al 2017 (in vivo)	R6/2 (160CAG) F, 10,12 wks. (n=4 & n=6)	ADC_W	4.7T	b= 136, 329, 675, 1035, 1481,1825	GM (CCX, pall)

				(s/mm²).	
(Vorisek et al., 2017)					
Gatto et al 2015b (ex vivo) ***(Gatto et al., 2015)***	R6/2 (160CAG) M&F, P30 (n=3 per group)	DTI	9.4T	b=1000 (s/mm²) 64dir	WM (CC genu)
Xiang et al 2011 (ex vivo) ***(Xiang et al., 2011)***	R6/2 (160CAG) M&F 12wks (n=3 per group)	DTI	11.7T	b=1500 (s/mm²) 6dir	WM (CC genu & Splenium)

Abbreviations: DTI, diffusion tensor imaging; CTWR, continuous random walk model; WM, white matter; GM, grey matter values, T, Tesla; dir, gradient direction; FA fractional anisotropy; AD, axial diffusivity; RD; radial diffusivity; MD; mean diffusivity; α, complexity coefficient; ADC_W, apparent diffusion coefficient of water; wks., weeks; P, post-natal day; cc. corpus callosum; ccx, cortex; pall, pallidum; ▲, increased compared to WT; ▼, decreased compared to WT.

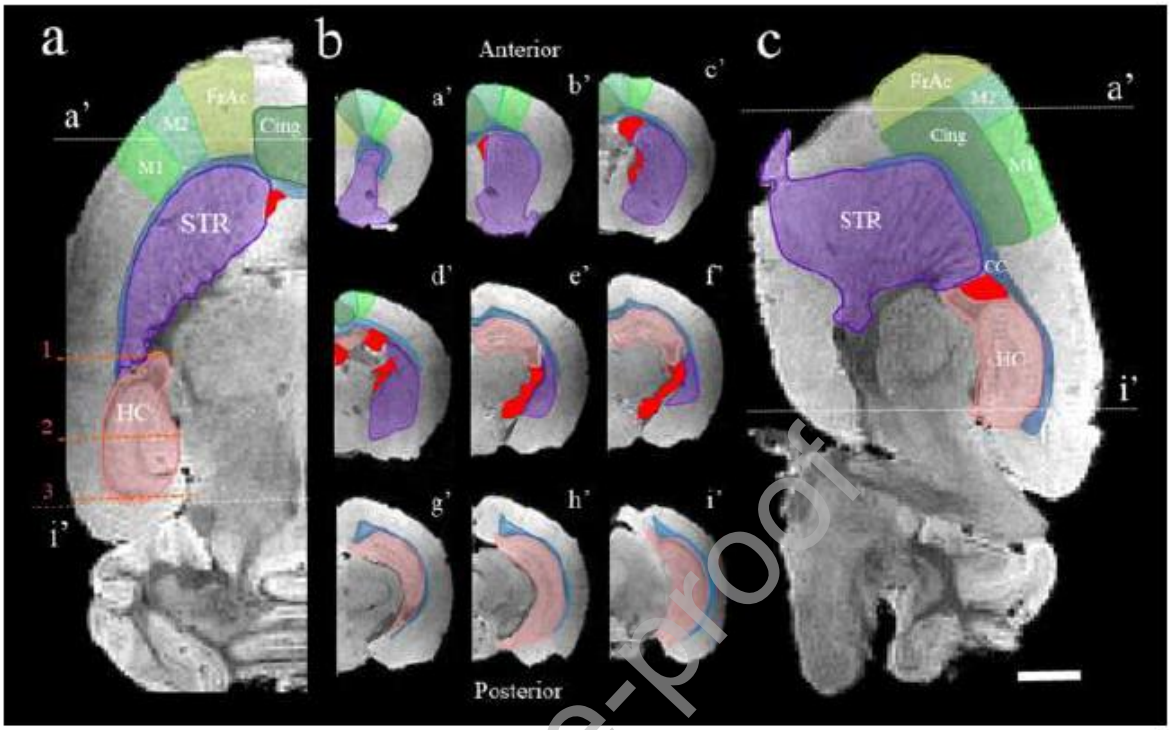

Figure 1 - *Regions of interest (ROIs) studied in the R6/1 mouse brain.* **Fig.1a -** Sagittal section of a mouse brain showing ROIs measured in a WT mouse at 16.7T and a 200 microns voxel resolution. **Fig.1b, c** - Coronal and longitudinal section of the same brain. Consecutive sections (a' anterior) to (i' posterior) are used to show the distribution of different white matter (WM) and grey matter (GM) structures. **Abbreviations:** FrAc, frontal accessory area; Cing, Cingular cortex area; M1, primary motor area; M2, Supplementary motor area; HC, hippocampus; STR, Striatal Area; CC, corpus callosum. Note that additional section's planes (1,2,3) are used to describe the anterior, medial, and posterior part of the hippocampus. Scale bar = 1mm

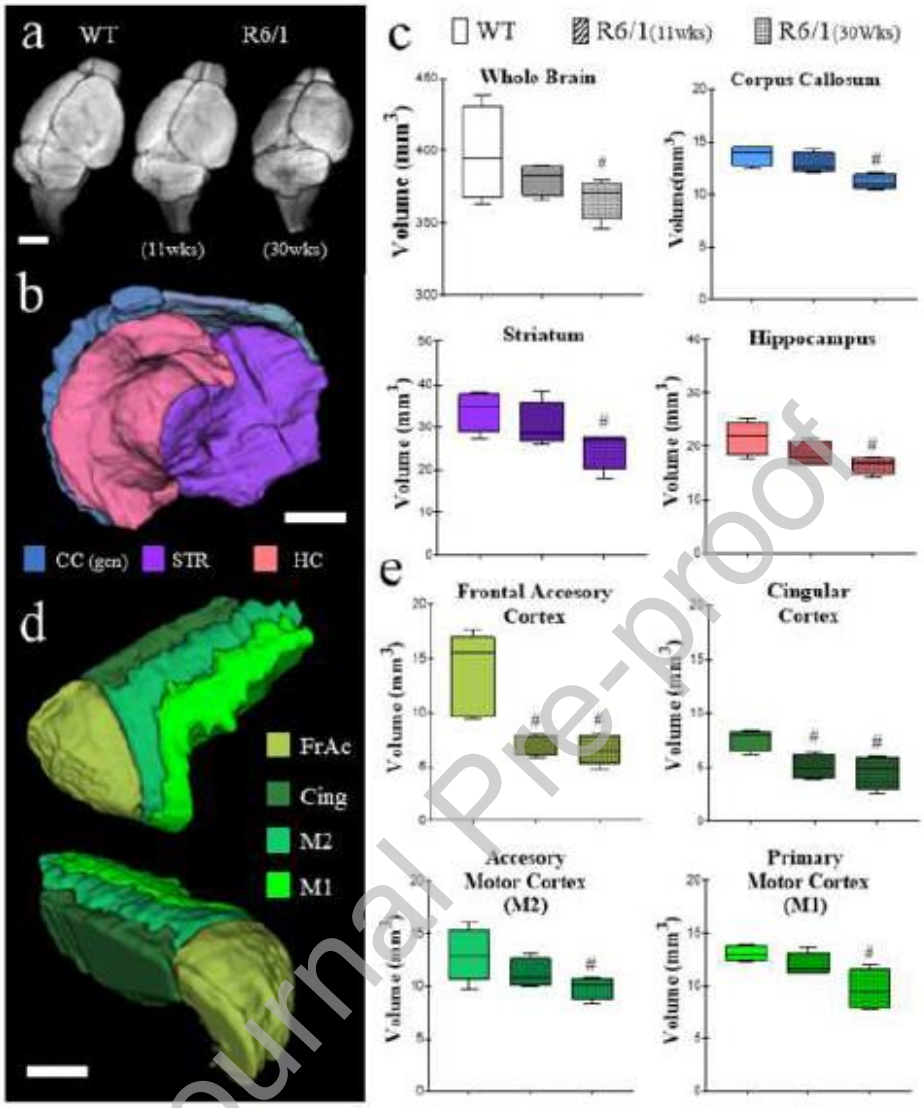

Figure 2 - *UHD-MRI MRI can capture early volumetric changes in specific GM cortical areas of the R6/1 mice.* **Fig.2a** - MRI Three-dimensional (3D) reconstruction of three representative mouse brains from the control wild type (WT) and Huntington disease mouse (R6/1) at the presymptomatic (11wks) and symptomatic stage (30wks). **Fig.2b, c** - Manual segmentation and 3D reconstruction of susceptible WM and GM areas of transgenic HD mouse brain R6/1. **Fig.2d** - Quantitative volumetric measure of the entire brain and areas segmented in the WM deep GM. Note that none of these areas has presymptomatic changes. **Fig.2e** Areas from superficial GM areas of the brain. Except for the frontal accessory cortical area, no significant difference between control and R6/1 mouse was detected in the presymptomatic stage of the disease. **Abbreviations:** FrAc, Frontal Accessory area; Cing, Cingular cortex area; M1, Primary Motor area; M2, Supplementary Motor area; HC, Hippocampus; STR, Striatal Area; CC, corpus callosum. Scale bar = 1mm. (n=4 per group), (# = $p<0.05$).

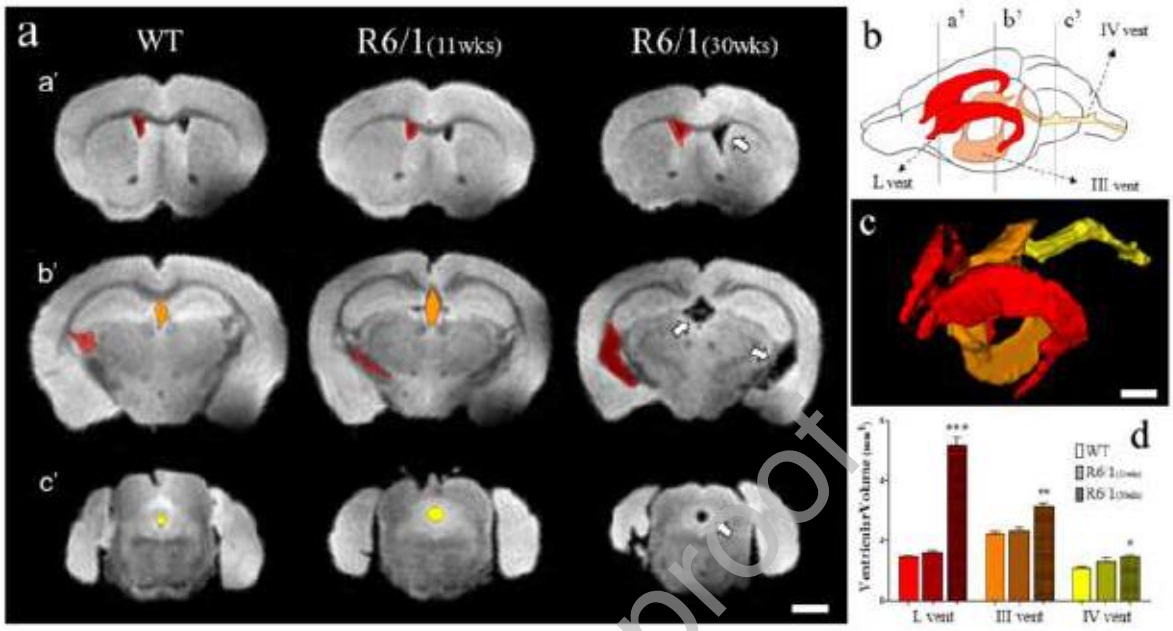

Figure 3 - *Enlargement of the R6/1 mice ventricular area cannot be detected in the early R6/1 mice model of HD*. **Fig.3a** -MRI coronal section from control (WT) and transgenic HD mouse brains (R6/1). Lateral ventricles are masked (red), third, and fourth ventricular systems are marked in orange and yellow respectively (arrows). **Fig. 3b** - Diagram of the ventricular system in the mouse brain showing the location of the coronal planes (a', b' and c') used in Fig.3a. **Fig.3c -** Three-dimensional reconstruction of the entire ventricular system in a WT mouse. **Fig.3d** - Quantitative volumetric analytics of the ventricular system. Note that no statistical changes in ventricular volumes can be detected between control and R6/1 mouse at the early stages. Abbreviation: L vent, lateral ventricles; III vent, third ventricle, and IV, fourth ventricle. Scale bar = 1mm. (# = $p<0.05$, ## = $p<0.01$, ### = $p<0.001$). (n=4 per group),

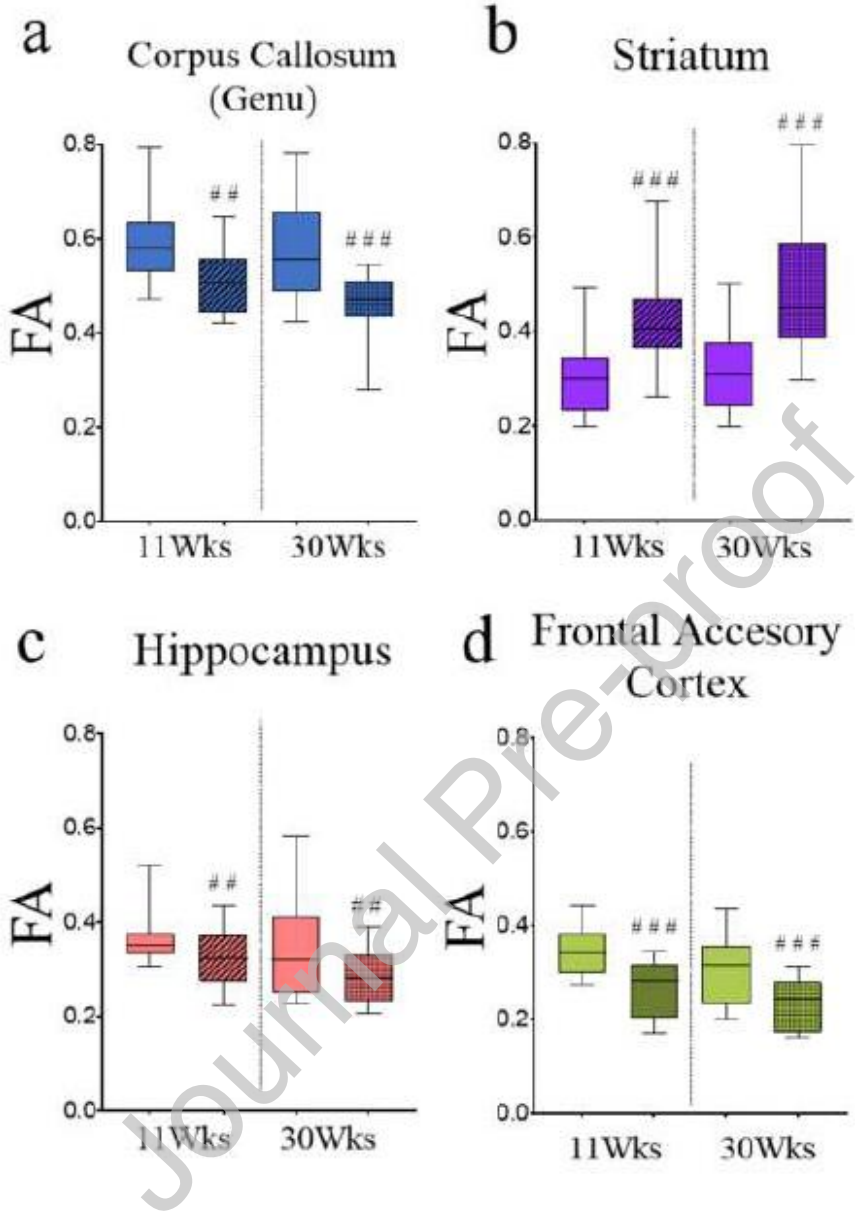

Figure 4 - *Fractional anisotropy (FA) dMRI sections show progressive microstructural changes in brain regions of interest.* Changes in FAs in the anterior part of the corpus callosum **(a)**, striatum **(b)**, Hippocampus **(c),** and frontal accessory areas **(d)**. One- way ANOVA and Tukey post-hoc comparison was established between WT-11wks & WT-30wk and their corresponding R6/1 mice groups at 11wks and 30wks). (# = $p<0.05$, ## = $p<0.01$, ### = $p<0.001$). (n=4 per group).

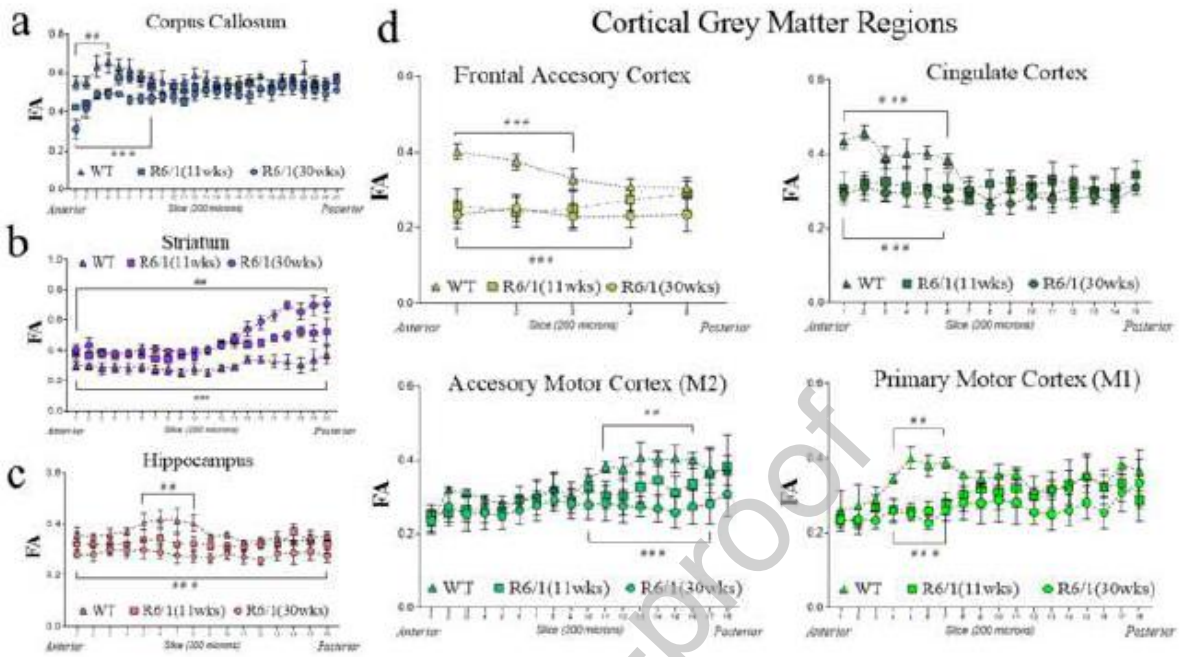

Figure 5 - *Analysis of consecutive spatial trends in fractional anisotropy (FA) dMRI sections shows progressive microstructural changes in different brain regions of the R6/1 mice.* **Fig. 5a** - FA changes along with the CC. Note that the anterior section (Genu) shows early changes. **Fig. 5b** - Contrary to other regions, FA changes in STR show an increasing trend as the disease progresses, predominantly in the posterior regions. **Fig. 5c** - An increase in the FA occurs in the medial section of the HC (see MRI section number 2 in Fig.1a) **Fig. 5d** - An earlier (11wks) and more anterior decrease in FA can be located in the FrAc and Cingular GM areas compared to M1 and M2 cortical areas of the R6/1 mouse. **Abbreviations:** FrAc, Frontal Accessory area; Cing, Cingular cortex area; M1, primary motor area; M2, Supplementary motor area; HC, hippocampus; STR, Striatal Area; CC, corpus callosum. **Upper brackets = (WT-11wks vs. R6/1-11wks. groups), lower brackets (WT-11wks vs R6/1 30 wks. groups)** (# = $p<0.05$, ## = $p<0.01$, ### = $p<0.001$). (n=4 per group).

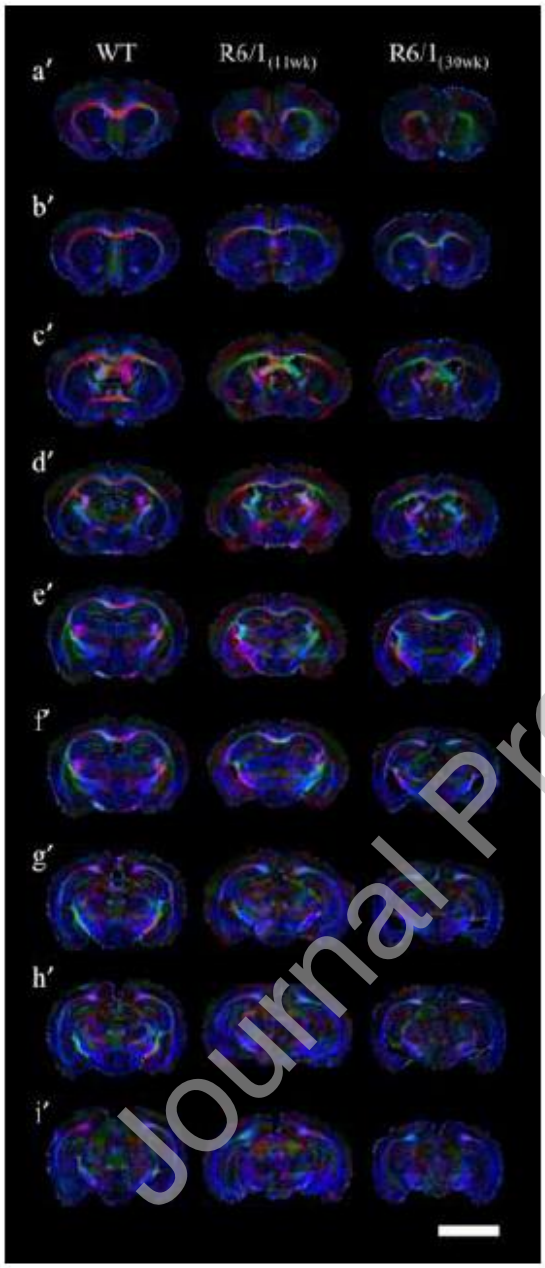

Figure 6 - A*nisotropic directional brain maps from coronal sections from diffusion tensor imaging (DTI) calculations in WT and R6/1 mice*. Differences between control and R6/1 mice brain's maps are due to changes in tissue microstructure changing the color encoded information eigenvectors' direction. Scale bar = 5mm.

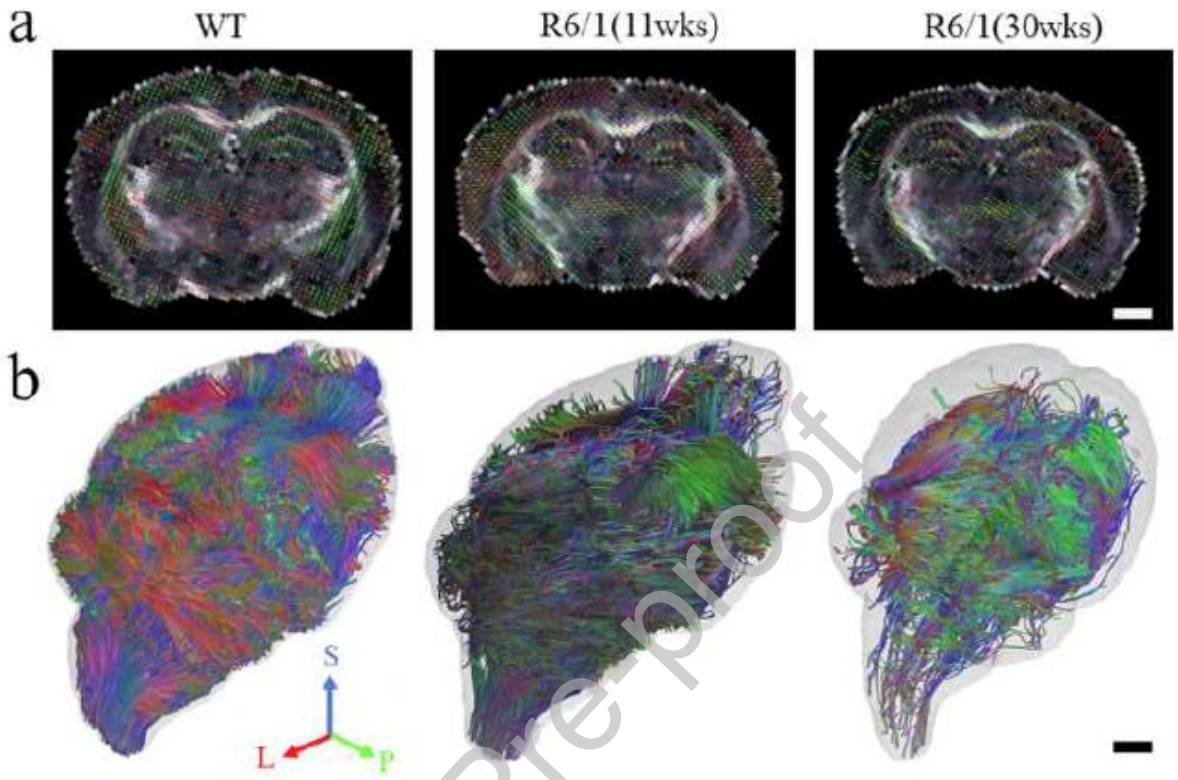

Figure 7 - *Global changes in axonal connectivity demonstrated by deterministic tractography reconstructions in the brain of the control and R6/1 mice*. **Fig.7a** - Coronal dMRI section mapping local fiber directions in the control and transgenic presymptomatic (R6/1 11wks) and symptomatic HD mice (R6/1 30wks). **Fig.7b** - Directionally color encoded tractography reconstructions showing a higher number of diffusion tracts in the WT mice compared to the R6/1 mice groups with a loss of neuronal connectivity as the disease progresses. **Abbreviations:** WT, wild type; R6/1, transgenic mice with Huntington's disease mutation; S, Superior; L, lateral; P, Posterior. Scale bar = 1mm.

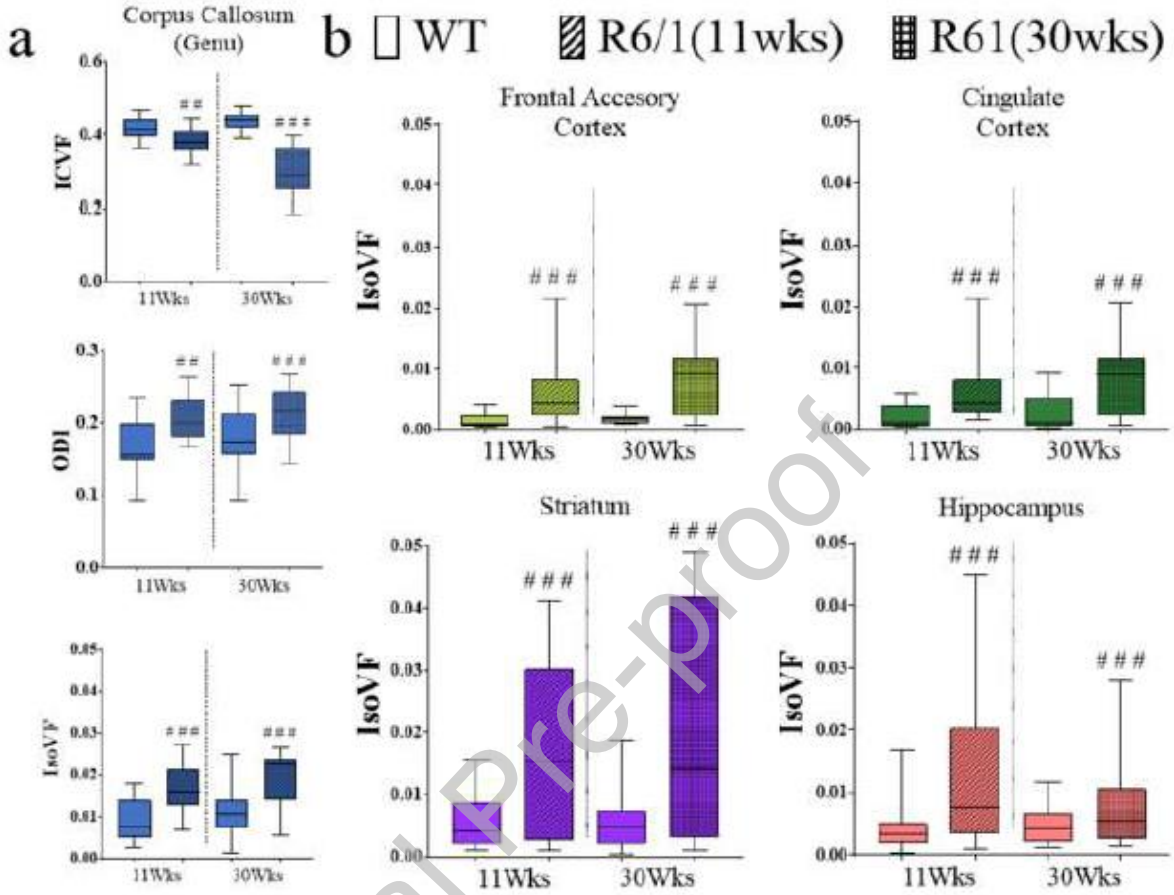

Figure 8- *Neurite Orientation Dispersion and Density Imaging model outputs from segmented ROIs brain in the R6/1 mice illustrate changes in different tissue compartments*. **Fig.8a** - A combined decrease in intracellular ventricular fraction (ICVF) and a rise in orientation dispersion index (ODI), as well as an isovolumetric fraction (IsoVF), can be seen in the anterior portion of the corpus callosum R6/1 mice (a main affected WM structure in HD). **Fig.8b** - Additional compartmental analysis in superficial (FrAc & Cing cortex) and deep (STR & HC) GM structures show a progressive increase in IsoVF. Note the broader changes in this parameter between WT and the R6/1 mice at the early stages of the disease. **Abbreviations:** WT, wild type; R6/1, transgenic mice with Huntington's disease mutation; WM, white matter; GM, grey matter; NODDI, Neurite Orientation Dispersion and Density Imaging; ICVF, Intracellular Ventricular Fraction; ODI, Orientation Dispersion Index; IsoVF, Isovolumic Fraction; FrAc, Frontal Accessory area; Cing, Cingular cortex area; HC, hippocampus; STR, Striatal Area; CC, corpus callosum. (# = $p<0.05$, ## = $p<0.01$, ### = $p<0.001$). (n=4 per group).

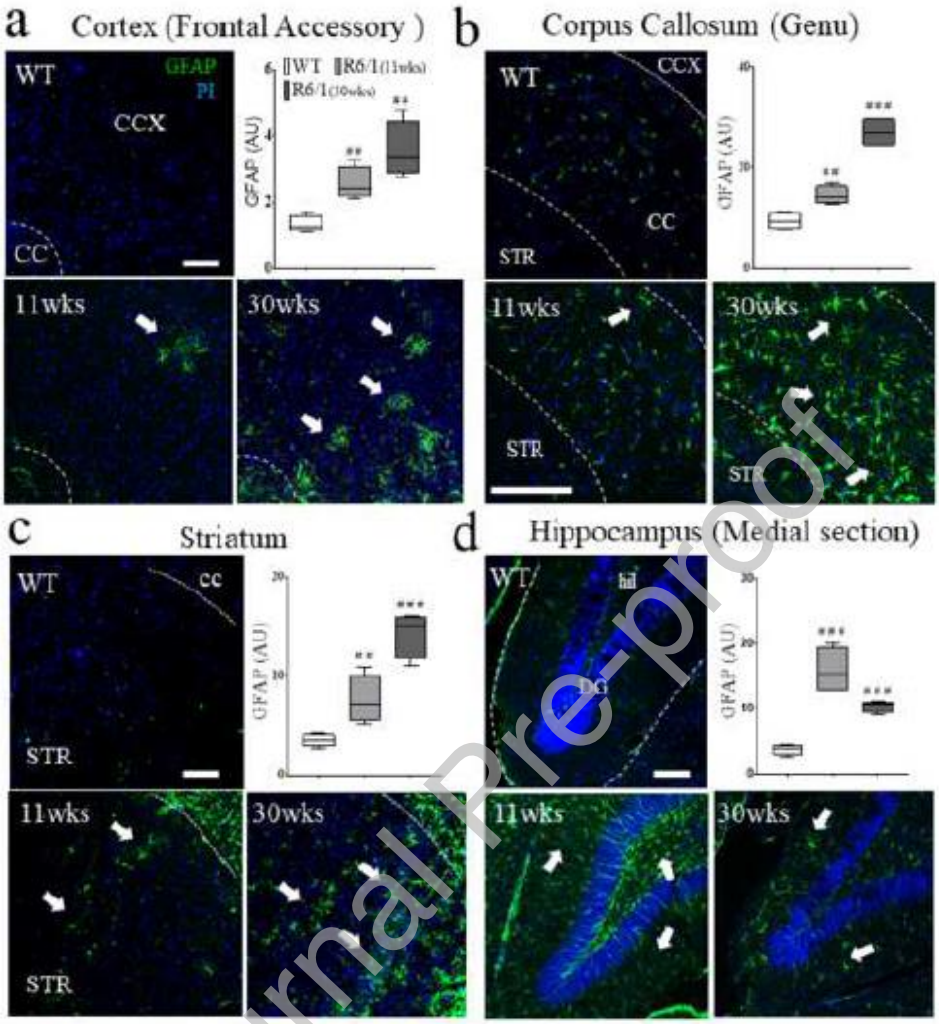

Figure 9 - *Astrocytic activated markers showed neuroinflammatory processes from the early stage of the disease in the R6/1 mice.* **Fig.9a** - Glial Fibrillary Acid Protein (GFAP) histochemical staining for the frontal accessory (FrAc) cortical area showing a statistically significant number of astrocytes (arrows) from presymptomatic to symptomatic stages in the R6/1 mice. **Fig.9b -** Progressive increase in astrocyte GFAP in the anterior portion (genu) of the corpus callosum (CC) particularly in the R6/1 at 11 and 30weeks. **Fig.9c** -Surge in striatal astrocytes labeled with GFAP (arrows) detected at the early and late stages of the disease. **Fig.9d** - Quantitative GFAP analysis centered in the hippocampal dental gyrus showed a greater increase in the presymptomatic R6/1 mice compared to the symptomatic mice group, marking a stronger and earlier inflammatory response of this deep GM structure. All scale bars = 10 microns. **Abbreviations:** FrAc, Frontal Accessory cortical area; ccx. cortex area; HC, hippocampus; STR, Striatal Area; CC, corpus callosum; hil., hilus; WT, wild type; a.u., arbitrary units; R6/1, transgenic mice with Huntington's disease mutation; GFAP, Glial Fibrillary Acid Protein; PI, Propidium Iodine. (# = $p<0.05$, ## = $p<0.01$, ### = $p<0.001$).

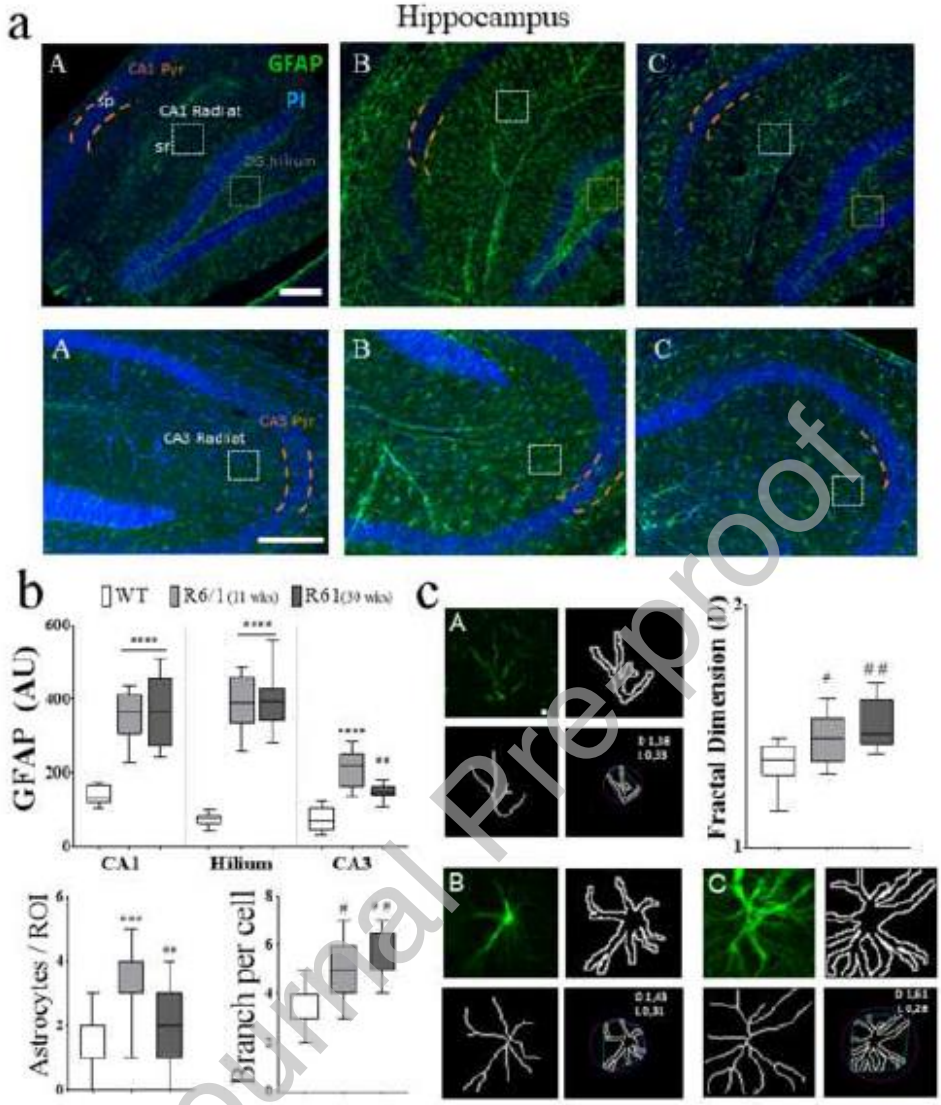

Figure 10 - *Summary of changes observed in the hippocampus of the transgenic R6/1 mice model determined by GFAP staining of astrocytes.* **Fig.10a -** Longitudinal sections stained against GFAP and using PI as a nuclear marker showing ROIs measured in a WT (A), R6/1 presymptomatic (B), and R6/1 symptomatic mouse at 10x (upper panel) and 20x (bottom panel) for proper visualization of the ROIs analyzed. **Fig.10b -**Representative plots of GFAP mean intensity of CA1, hilus, and CA3 as described in a. and quantification of astrocytes per ROIs and branches/cell in CA3 (bottom). **Fig.10c -** Representative images of astrocytes from CA3 str Rad of WT (A), R6/1 presymptomatic (B), and R6/1 symptomatic mouse analyzed to obtain a binary image, and outline, skeleton, and the convex hull and minimum bounding circle diagram with parameters (D, fractal dimension, and L, lacunarity) obtained via the plugin FracLac through image J as described in materials and methods. The plot shows the mean of Fractal Dimension (D) obtained for each condition. Notice the increase in D (complexity) in R6/1 animals compared to WT. **Abbreviations**: CA, Cornu Ammonis; pyr, pyramidalis; sr, strata radiatum; sp strata pyramidalis; D, fractal dimension; L, lacunarity; AU, Arbitrary Units; Scale bar = 1mm.

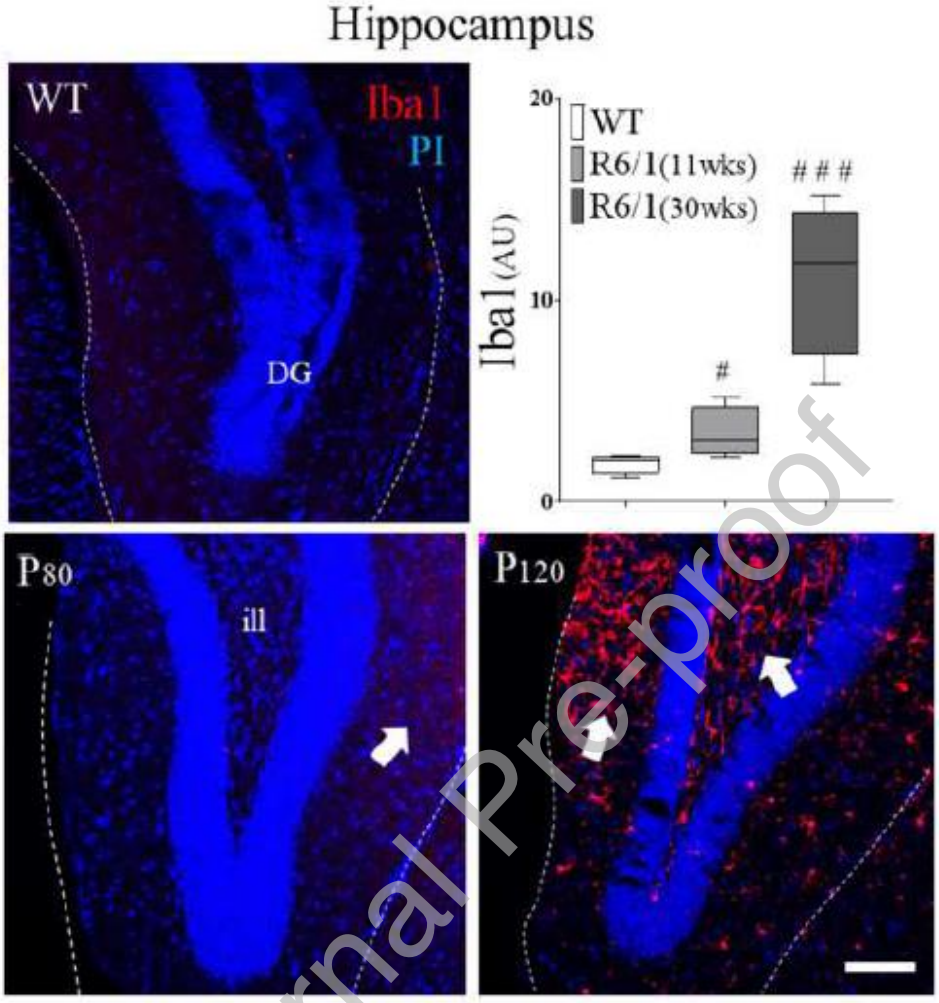

Figure 11 – *Iba1 marker showed a progressive increase in microglia activity in the deep regions of the R6/1 mouse hippocampus.* Quantitative analysis of the R6/1 mouse hippocampal dental gyrus (DG) illustrates a progressive increase in microglia infiltration (arrows) with a maximum level at the symptomatic stage (30 weeks). Scale bar = 10 microns. **Abbreviations:** WT, wild type; a.u., arbitrary units; R6/1, transgenic mice with Huntington's disease mutation; Iba1, microglia cell markers; DG, Dental gyrus; Ili., hippocampus's ilium; PI, Propidium Iodine. (# = $p<0.05$, ## = $p<0.01$, ### = $p<0.001$).

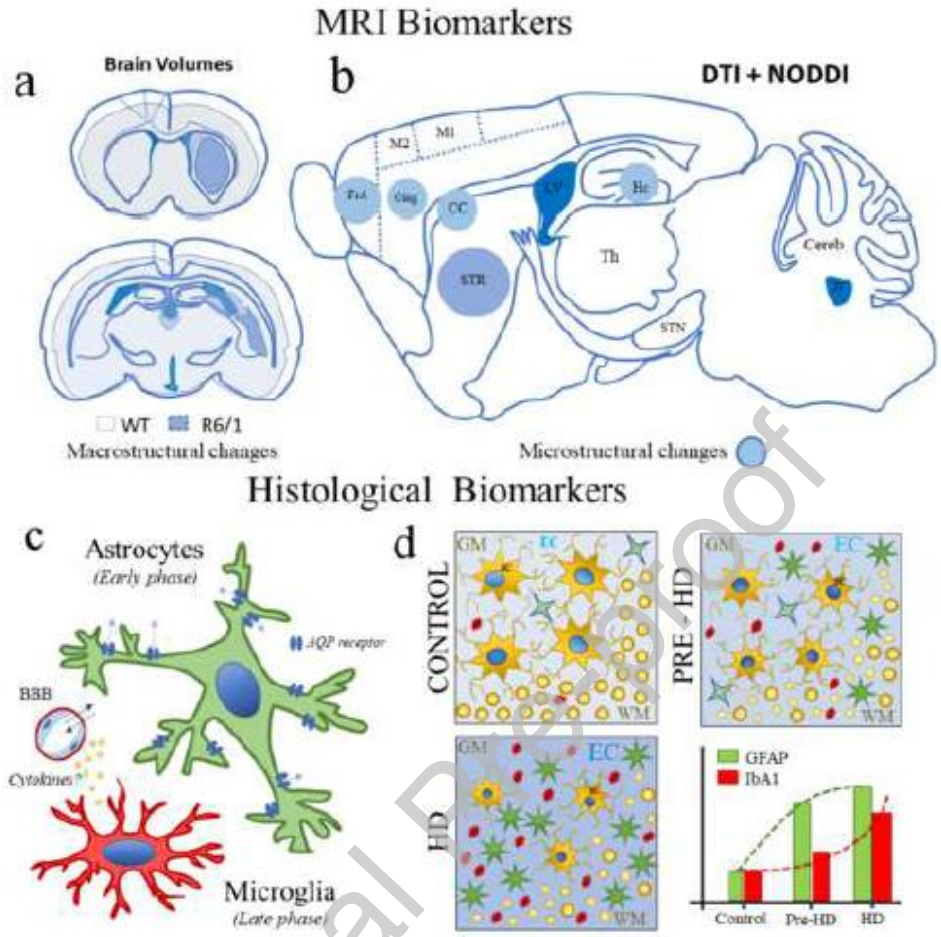

Figure 12 - *Summary of changes observed in brain tissue of the transgenic R6/1 mice model captured by diffusion MRI and histopathological markers of neuroinflammation.* **Fig.12a -** Macrostructural biomarkers derived from MRI scans showed a significant reduction in volume across regions, particularly susceptible to the mHTT expression. Significant changes in whole brain volume and segmented ROIs can only be detected at the symptomatic stage. **Fig.11b -** Microstructural changes can be measured in specific regions of the R6/1 mouse neuroanatomy. In such regions, early changes in GM and WM neuronal microstructure can be analyzed by applying diffusion tensor imaging (DTI). In WM tracts (represented as axonal cross-sections in fig 11d) and cortical GM, a significant decrease in fractional anisotropy (FA) can be associated with a neuronal injury. Neurodegenerative microstructural changes detected with the Neurite Orientation Dispersion and Density Imaging (NODDI) model using the cell degeneration and neuronal mass intracellular compartment (IC) and the intracellular volume fraction (ICVF). **Fig.12c -** Glial cells like astrocytes and microglia have a major role in the regulation of the brain tissue microenvironment. **Fig.12d -** Astrocytes (by their regulation of the membrane Aquaporin receptor expression) regulate the hydric environment. Water balance mechanisms could be altered or enhanced in the early stages of HD. Thus, the combination of neurite volume decreases and a potential increase in water content could explain the expansion of the extracellular compartment (EC), increasing the overall mean diffusion (MD) within the voxel, as well as the orientation diffusion index (ODI). Also, microglial cells, (one of the main cells involved in inflammatory processes) increases their secretion of cytokine

mediators, also augmenting the tissue water permeability from the brain-blood barrier (BBB) at later stages of the disease. The combination of all previously mentioned effects (decrease in the IC, increase in EC, and small vessel permeability) may lead to an early and local (interstitial) raise in free-water content, as detected by an increase in the levels of isotropic volume fraction (IsoVF). **Abbreviations;** WT, wild type; R6/1, a transgenic mouse with Huntington's mutation HD, Huntington's Disease; FrA, frontal accessory area; Cing, Cingular cortical area; M1, primary motor area; M2, secondary motor area, CC, Corpus Callosum; STR, Striatum, HC hippocampus; Cereb., cerebellum; STN, o subthalamic Nucleus Th, thalamus; LV, lateral ventricle; IV, Fourth ventricular system, BBB, Brain blood Barrier; AQP; aquaporin receptor; Pre-HD; Presymptomatic stage of Huntington's disease; HD, Huntington's disease; GM, grey Matter; WM, white matter; IC, intracellular compartment; EC, extracellular compartment; GFAP, astrocyte marker; Iba1, microglial marker; NODDI, Neurite Orientation Dispersion and Density Imaging; ICVF, Intracellular Ventricular Fraction; ODI, Orientation Dispersion Index; IsoVF, Isovolumetric Fraction

GRAPHICAL ABSTRACT

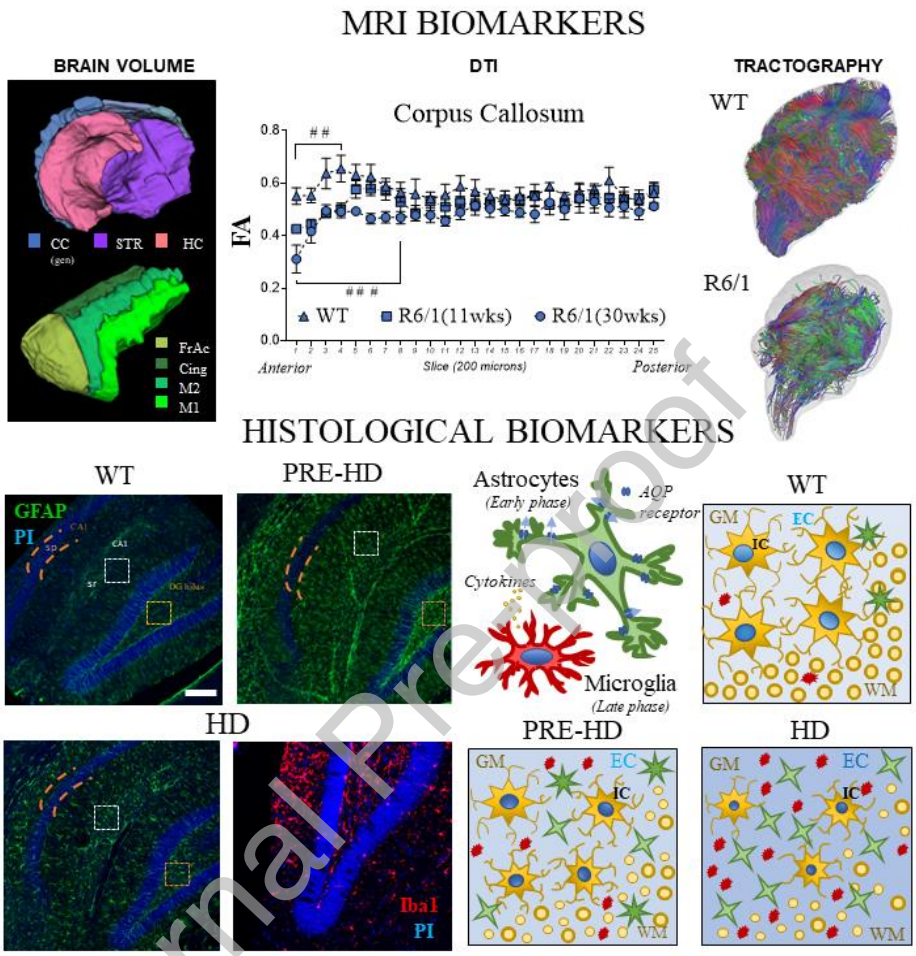

LEGEND

Ultra-high field diffusion MRI can detect brain structural changes in the Huntington s disease (HD), R6/1 mouse model. Diffusion tensor imaging (DTI) can capture early microstructural changes across different brain structures. dMRI parameters can be linked to cellular neuroinflammatory markers at an early stage of HD.